

Presentation and discussion of the high resolution atmosphere-land surface-subsurface simulation dataset of the **simulatedvirtual** Neckar catchment for the period 2007-2015

Bernd Schalge¹, Gabriele Baroni², Barbara Haese³, Daniel Erdal⁴, Gernot Geppert⁵, Pablo Saavedra¹, Vincent Haefliger¹, Harry Vereecken^{6,7}, Sabine Attinger^{8,9}, Harald Kunstmann^{3,10}, Olaf A. Cirpka⁴, Felix Ament¹¹, Stefan Kollet^{6,7}, Insa Neuweiler¹², Harrie-Jan Hendricks Franssen^{6,7}, Clemens Simmer^{1,7}

¹Institute for Geosciences, University of Bonn, Bonn, Germany

² Department of Agricultural and Food Sciences, University of Bologna, Bologna, Italy

³Institute of Geography, University of Augsburg, Augsburg, Germany

⁴Center for Applied Geoscience, University of Tübingen, Tübingen, Germany

⁵Department of Meteorology, University of Reading, Reading, England

⁶Forschungszentrum Jülich GmbH, Agrosphere (IBG-3), Jülich, Germany

⁷Centre for High-Performance Scientific Computing (HPSC-TerrSys), Geoverbund ABC/J, Jülich, Germany

⁸Institute of Earth and Environmental Science, University of Potsdam, Potsdam, Germany

⁹Helmholtz-Center for Environmental Research, Leipzig, Germany

¹⁰Institute of Meteorology and Climate Research (IMK-IFU), Karlsruhe Institute of Technology (KIT), Garmisch-Partenkirchen, Germany

¹¹Meteorological Institute, University of Hamburg, Hamburg, Germany

¹²Hannover, Institut für Strömungsmechanik und Umweltphysik im Bauwesen, Leibniz Universität Hannover, Germany

Correspondence to: Bernd Schalge (bschalge@uni-bonn.de)

Abstract.

Coupled numerical models, which simulate water and energy fluxes in the subsurface-land surface-atmosphere system in a physically consistent way are a prerequisite for the analysis and a better understanding of heat and matter exchange fluxes at compartmental boundaries and interdependencies of states across these boundaries. Complete state evolutions generated by such models may be regarded as a proxy of the real world, provided they are run at sufficiently high resolution and incorporate the most important processes. Such a **simulatedvirtual** reality can be used to test hypotheses on the functioning of the coupled terrestrial system. Coupled simulation systems, however, face severe problems caused by the vastly different scales of the processes acting in and between the compartments of the terrestrial system, which also hinders comprehensive tests of their realism. We used the Terrestrial Systems Modeling Platform TerrSysMP, which couples the meteorological model COSMO, the land-surface model CLM, and the subsurface model ParFlow, to generate a **simulatedvirtual** catchment

32 for a regional terrestrial system mimicking the Neckar catchment in southwest Germany. Simulations for this catchment are
33 made for the period 2007-2015, and at a spatial resolution of 400m for the land surface and subsurface and 1.1km for the
34 atmosphere. Among a discussion of modelling challenges, the model performance is evaluated based on ~~real~~-observations
35 covering several variables of the water cycle. We find that the simulated-~~(virtual)~~ catchment behaves in many aspects quite
36 close to observations of the real Neckar catchment, e.g. concerning atmospheric boundary-layer height, precipitation, and
37 runoff. But also discrepancies become apparent, both in the ability of the model to correctly simulate some processes which
38 still need improvement such as overland flow, and in the realism of some observation operators like the satellite based soil
39 moisture sensors. The whole raw dataset is available for interested users. The dataset described here is available via the
40 CERA database (Schalge et al, 2020): https://doi.org/10.26050/WDCC/Neckar_VCS_v1
41

42 1 Introduction

43 Earth environmental models are becoming increasingly important for climate and weather prediction, flood forecasting,
44 water resources management, agriculture, and water quality control (e.g. Shrestha et al. 2014; Larsen et al. 2014; Simmer et
45 al., 2015). Assuming that that the models are able to resemble the real-world based on state-of-the-art understanding of the
46 system processes, the models are also used as “virtual realities” for hypothesis testing and decision support systems in many
47 scientific disciplines (Clark et al., 2015, Semanova & Beven, 2015).

48 Virtual ~~or simulated~~ realities have been used for specific compartments of the terrestrial system in many studies (see Fatichi
49 et al., 2016, and reference herein) and several advantages have been recognized. Bashford et al. (2002) computed
50 ~~simulated~~~~virtual~~ remote-sensing observations with 1 km resolution to derive, among others, process parameterizations for
51 evapotranspiration in a hydrological model operating on the same scale as the remote sensing data. Weiler and McDonnel
52 (2004) used a ~~simulated~~~~virtual~~-reality approach on the hill-slope scale to detect and quantify the major controls on
53 subsurface flow processes and derive tunable parameters for conceptual models. ~~Similar~~~~Virtual~~ experiments allowed
54 Schlueter et al. (2012) to explore the relationship between soil architecture and hydraulic behavior and Chaney et al. (2015)
55 to testing sampling designs. Hein et al. (2019) explores the relative importance of different factors in the hydrologic response
56 of a catchment. ~~Simulated~~~~Virtual~~ realities are also often used to overcome limitations on the data-scarce observations. In this
57 context, Ajami and Sharma (2018) used simulations results to test disaggregation method for soil moisture observations. In
58 subsurface hydrology it is a standard procedure to test inverse modeling and data-assimilation approaches on
59 ~~simulated~~~~virtual~~ aquifers (e.g., Zimmermann et al., 1998; Hendricks Franssen et al., 2009), which are used to generate
60 realistic aquifer data with exactly known hydraulic and geochemical properties at every point (e.g., Schaefer et al., 2002).
61 More recently, it has been highlighted that the terrestrial systems should be better exploited by the use of integrated models
62 which are able to simulate water and energy fluxes in the subsurface-land surface-atmosphere system in a physically
63 consistent way (Clark et al., 2015, Davison et al, 2018). For this reason, these integrated modeling approaches have also

64 | been considered to generate simulatedvirtual realities (Mackay et al., 2015). However, despite the increasing computational
65 | capability and availability of infrastructures, these modelling approaches are generally more technically demanding. In
66 | addition, the use of these types of integrated models requires different expertises that are not usually cover within one single
67 | scientific group but requires strong interdisciplinary collaborations among different partners. For these reasons, the use of
68 | these types of models is still not commonly foreseen.

69 | To overcome this limitation, in this paper we present the development, the testing and the data of a simulatedvirtual reality of
70 | a mesoscale catchment based on a fully integrated terrestrial model system. Our simulatedvirtual catchment encompasses the
71 | terrestrial system from the bedrock to the upper atmosphere covering the catchment of a higher-order river (length \approx 380km,
72 | area \approx 14000km²) including a buffer zone surrounding it, in which we simulate - as realistically as currently possible - the
73 | multi-year evolution of states including the water and energy fluxes in and between all its compartments. We specifically
74 | venture to represent the strong spatial variability of the land components, which affects the overall system behavior due to
75 | nonlinear couplings and feedbacks. Since a simulatedvirtual catchment with no resemblance to a real world catchment hardly
76 | allows for evaluating its realism, we base our simulation loosely on the Neckar catchment in southwest Germany that
77 | contains quite variable topography, different land cover, high and low precipitation regions, deep and shallowlow water
78 | tables and regions prone to flooding events. (see Figure 1). The model does not aim at exactly reproducing the catchment's
79 | response to hydro-climatic forcing, instead we only require that the simulated response is realistic with respect to typical
80 | spatial and temporal characteristics. For this reason, we discuss the model realism in comparison with observations of the
81 | real catchment, but also its limitations, particularly in relation to the chosen resolutions which balance the detail in process
82 | representation and computational feasibility. Despite these simplifications we believe this dataset will be useful in a variety
83 | of ways, such as data assimilation, model comparison studies and model development studies as well as focused impact
84 | studies. In the discussion section at the end we go more into detail how this dataset can potentially be used and what the
85 | limits of applicability are.

86 | The remainder of the paper is structured as follows. In section 2, we introduce the simulation platform TerrSysMP, while
87 | Section 3 describes in detail the surface and subsurface parameters for topography, soils and aquifers, land use, vegetation,
88 | and the river network. In Section 4, we show snapshots and time series of state variables or system parameters extracted
89 | from the simulatedvirtual catchment and compare them to observations in the real Neckar catchment to demonstrate how
90 | well the most important requirements are met. These results as well as possible ways to improve them are discussed in
91 | Section 5 together with several issues, which came up during the development phase. We provide conclusions and an
92 | outlook in Section 6.

93 | **2 The Terrestrial Systems Modeling Platform (TerrSysMP)**

94 | We used the Terrestrial System Modeling Platform (TerrSysMP, see Shrestha et al. 2014; Gasper et al. 2014; Sulis et al.
95 | 2015) developed within the Transregional Collaborative Research Centre TR32 (Simmer et al. 2015) for the generation of

96 | the ~~simulated~~^{virtual} catchment. TerrSysMP couples (Figure 1 in [Gasper et al., 2014](#)) the hydrologic flow model ParFlow
97 v693 (Ashby and Falgout, 1996; Jones and Woodward, 2001; Kollet and Maxwell, 2006), the land-surface model
98 Community Land Model, CLM v3.5 (Oleson et al., 2008), and the atmospheric model Consortium for Small Scale Modeling
99 (COSMO v4.21, Baldauf et al., 2011) via the Ocean Atmosphere Sea Ice Coupling framework OASIS3 (e.g. Valcke et al.,
100 2006), using a dynamical two-way approach including down- and upscaling algorithms for fluxes and state variables
101 between computational grids of different resolution.

102 ParFlow is a variably saturated watershed flow model, which solves the three-dimensional Richards equation to model
103 saturated and unsaturated flow in the subsurface, and the fully integrated kinematic wave equation to model two-dimensional
104 overland flow. Also other global and regional hydrological models use the latter to route overland flow, e.g. MODCOU
105 (Haefliger et al., 2015) and TRIP (Alkama et al., 2012). Advanced Newton-Krylov multigrid solvers are used that are
106 especially suitable for massively parallel computer environments. Excellent model performance and parallel efficiency have
107 been documented by Jones and Woodward (2001), Kollet and Maxwell (2006), and Kollet et al. (2010). A unique feature of
108 ParFlow is the use of an advanced octree data structure for rendering overlapping objects in 3-D space, which facilitates
109 modeling complex geology and heterogeneity as well as the representation of topography based on digital elevation models
110 and watershed boundaries.

111 CLM is a single column biogeophysical land-surface model released by the National Center for Atmospheric Research
112 (NCAR), which considers coupled snow, soil, and vegetation processes. Land surface heterogeneity is represented as a
113 nested sub-grid hierarchy in which grid cells are composed of multiple land units (glacier, lake, wetland, urban, and
114 vegetation), snow/soil columns (to capture variability in snow and soil states within each land unit), and Plant Functional
115 Types (PFTs) to capture the biogeophysical and biogeochemical differences between broad categories of plants in terms of
116 their functional characteristics. In TerrSysMP, the 1-D Richards-equation model included in CLM is replaced by ParFlow.

117 COSMO is a limited-area, non-hydrostatic numerical weather prediction model, which operationally runs at the German
118 weather service DWD, among others, for Numerical Weather Prediction (NWP) and various scientific applications on the
119 meso- β and meso- γ scale. COSMO is based on the primitive thermo-hydrodynamical equations describing compressible
120 flow in a moist atmosphere. As a limited-area model, COSMO needs lateral boundary conditions from a driving larger-scale
121 model. We impose the lateral conditions by nesting COSMO in COSMO-DE which spans Germany. At the lateral
122 boundaries a relaxation technique is used in which the internal model solution is nudged against an externally specified
123 solution over a narrow transition zone between the two domains. Version 3.5 of CLM that is used here is already relatively
124 old. Even though version 5 was not yet available when we started our work, it is now and comparison is warranted. Newer
125 versions of CLM have several major improvements over 3.5. The first one is a more sophisticated routing scheme leading to
126 much improved soil moisture profiles. In our case we replace this part with ParFlow anyway so our older version is not a
127 disadvantage in that regard. Other improvements are the inclusion of carbon and nitrogen cycles as well as more options for
128 crop type vegetation. Here we purposely simplify our setup as we not only have and want static land use but also use a blend
129 type of crop with no sharp changes in LAI due to harvests. Instead, we assume harvest to be an ongoing process all

130 throughout autumn. Thus, all these improvements do not downgrade the simulation results presented and discussed in this
131 study.

132 Within OASIS3, the upscaling algorithm uses the mosaic or explicit sub-grid approach (Avisar and Pielke, 1989) in which
133 high-resolution land surface fluxes are averaged and transferred to the coarser resolution of the atmospheric model
134 component. The implemented Schomburg scheme (Schomburg et al., 2010, 2012) downscales atmospheric variables of the
135 lowest atmospheric model layer to the higher-resolved land surface model. The scheme involves (i) spline interpolation
136 while conserving mean and lateral gradients of the coarse field, (ii) deterministic downscaling rules to exploit empirical
137 relationships between atmospheric variables and surface variables, and (iii) the addition of high-resolution variability (i.e.
138 noise) in order to honor the non-deterministic part and to restore spatial variability.

139 TerrSysMP allows simulating the terrestrial water, energy, and biogeochemical cycles from the deeper subsurface including
140 groundwater (ParFlow) across the land-surface (CLM) into the atmosphere (COSMO). Water and energy cycles are coupled
141 via evaporation and plant transpiration; these processes are modeled by CLM with a non-linear coupling to ParFlow through
142 soil-water availability and root-water uptake (Figure 2). The two-way coupling between CLM and COSMO encompasses
143 radiation exchange and turbulent exchanges of moisture, energy, and momentum. OASIS3 allows for different temporal and
144 spatial resolutions of the coupled model components. For example, a temporal resolution of 15 minutes is sufficient for the
145 subsurface and land-surface components, whereas time steps as small as 5 seconds are needed for the atmosphere. A higher
146 spatial resolution can be assigned for the surface and subsurface parts to allow for a better representation of soil and land-use
147 heterogeneity.

148 Since high-resolution and long time-series of the fully coupled system are needed to satisfy our need to check the statistical
149 behavior of the system, the models were run on the IBM/BlueGeneQ System JUQUEEN at the Jülich Supercomputing
150 Centre (Jülich Supercomputing Centre, 2015). JUQUEEN has a total of 28672 nodes with 16 cores each. Our configuration
151 involved using 256 nodes for 12hours, restarting the simulation every 7 simulation days. This is necessary as the runtime for
152 Parflow can vary greatly depending on the conditions in the ~~virtual~~ catchment. The total number of grid cells for the domain
153 is 323,675 per model layer with 10 layers for CLM and 50 layers for ParFlow, and 58,420 grid-points for the 50 COSMO
154 layers resulting in 22.3 million grid cells. We ran the fully-coupled model for a total period of nine years (2007-2015) as
155 2007 was the first full year where high resolution atmospheric forcing was available and nine years was the maximum
156 possible length with our granted compute time. On average the actual runtime was approximately eight hours. This means
157 that for one year of simulation ~~roughly about~~ 1.7 million core-hours are needed. For the full nine-year time-series that is
158 about 12 million core-hours; another ~8 million hours were needed for the spin-up. We used an output interval of 15
159 minutes, which results in a total output of 38.5TB of data for the full time-series, where about half was produced by COSMO
160 and a quarter each by CLM and ParFlow.

161 | 3 Description of the SimulatedVirtual Catchment

162 | Our simulatedvirtual catchment is based on the Neckar catchment in southwestern Germany (see Figure 1), east of the Black
163 | Forest mountain range and north of the Jurassic ridge of the Swabian Alb. The catchment has a varying topography including
164 | mountains up to 1050 m a.s.l., river valleys, different land use types, i.e. grassland, cropland (majority of the area), broadleaf
165 | and needle leaf forest (see Figure 3), and relatively large soil spatial variability. Annual mean precipitation over the real
166 | catchment ranges between 500 and 2000mm (see Section 5.1) with highest values over the Black Forest. Inter-annual
167 | variability of precipitation can reach up to one third of the mean value. Monthly precipitation can vary largely and its mean
168 | annual cycle is weak with slightly lower values in spring and autumn. While summer precipitation is dominated by
169 | convection, winter precipitation is predominantly related to fronts of extra-tropical cyclones with enhanced precipitation
170 | over the mountains due to orographic lift. Daily average temperatures vary with altitude between -5°C and 0°C in January
171 | and between 13 and 18°C in July. Land use and cover in the lower elevations are dominated by agriculture while the Black
172 | Forest features mainly needle-leaf trees. Broad-leaf trees can be found over smaller areas throughout the catchment. The
173 | distance to groundwater is in large parts of the area restricted to a few meters, in particular in lowland areas, which assures
174 | strong coupling between groundwater table and evapotranspiration (Maxwell et al., 2007). These typical central European
175 | catchment features led us to choose the Neckar catchment as the basis for the simulatedvirtual catchment.

176 | The computational domain is a rectangular area of ~57,850km² encompassing the Neckar catchment of ~14,000km². The
177 | domain is larger than the Neckar catchment in order to allow the atmospheric model to develop its own internal dynamics.
178 | COSMO is run on a 1.1km horizontal grid with 230x254 grid points, which includes a 4 grid point-wide outer frame zone
179 | where only the lateral boundary forcing is used without coupling to the CLM, as well as 50 vertical layers in hybrid
180 | coordinates (terrain following at the surface, flat in the stratosphere). COSMO is set up identical to the operational COSMO-
181 | DE setup of the German national weather service (Deutscher Wetterdienst, DWD), e.g., the deep convection
182 | parameterization is switched off because at the chosen grid resolution convection is enabled by the dynamical core (see
183 | Section 2.1). In COSMO-DE, the operational resolution is 2.8km, so that the approximation regarding deep convection is
184 | even more appropriate in our simulations. Similar choices were taken by Smith et al. (2015), who simulated precipitation
185 | events of roughly the same domain using nested WRF models, where the cumulus parameterization was switched off at
186 | horizontal resolutions of 900m and 300m. Lateral boundary forcing and constant fields (topography, land-mask etc.) are
187 | provided by the COSMO-DE analysis fields, which are downscaled to the 1.1km grid by linear interpolation. The lateral
188 | relaxation zone, which moderates the jump from the lateral driving fields to the inner model area, is set to 12km.

189 | A software restriction (unfixable bug specific to the system we were running on) does not allow for cases with more than 4.2
190 | million CLM columns as the model does not initialize properly and crashes; thus, ~~thus~~ currently a higher spatial resolution
191 | for CLM and ParFlow than 400 m cannot be used for the Neckar catchment on the used system. So, ParFlow and CLM use
192 | the same horizontal grid with a resolution of 400 m and 535x605 grid points. The vertical grid for both component models is
193 | partially the same, with CLM limited to 10 vertical layers up to a total depth of 3 m shared with ParFlow, which has in total

194 50 vertical layers reaching down to 100m. COSMO runs with a 5sec timestep while CLM and Parflow run at 15min
195 timesteps, which is also the coupling frequency.

196 For setting up CLM, the European digital elevation model (DEM) by the European Environment Agency EEA
197 (<http://www.eea.europa.eu/data-and-maps/data/eu-dem>) was projected to the latitude/longitude grid and bi-linearly
198 interpolated to 400m from the original 30m spatial resolution. The same DEM is used to create the slope input files for
199 ParFlow. A slight modification to the original DEM was made in order to ensure that the simulated Neckar River would flow
200 in the correct valley, especially in the upper half of the catchment where the valley is not always properly resolved by the
201 400m resolution. In total, the elevation of 8 grid points was reduced to achieve proper routing for the Neckar River. [The](#)
202 [resulting elevation map is part of the CLM input data and available with the dataset as supplementary material.](#) We have not
203 considered rivers outside the Neckar catchment in these corrections; thus, there are cases where their routing is not identical
204 to the real rivers.

205 Land use is taken from the 2006 Corine Land Cover Data Set ([http://www.eea.europa.eu/data-and-maps/data/corine-land-](http://www.eea.europa.eu/data-and-maps/data/corine-land-cover-2006-raster-3)
206 [cover-2006-raster-3](http://www.eea.europa.eu/data-and-maps/data/corine-land-cover-2006-raster-3)) also provided by EEA. Since the latter dataset features many more land use types (at a resolution of
207 100m) than required by CLM, they were grouped according to the CLM (IGBP) Plant Functional Type classes (1) broad-leaf
208 forests, (2) needle-leaf forests, (3) grassland, (4) cropland, and (5) bare soil. Urban areas are not considered in this setup and
209 replaced by bare soil. Water surfaces (e.g., larger lakes like Lake Constance in the South of the domain) are also treated as
210 bare soil in CLM while COSMO uses its own land-mask and specific calculations for water surfaces. Therefore, no values
211 from CLM are used for water surfaces in COSMO. A few hundred grid cells feature shrubs (mostly areas that are re- or de-
212 forested or areas at higher altitudes) which are treated as forests, and each grid cell features only one – the most dominant –
213 plant functional type. The plant Leaf Area Index (LAI) is computed from MODIS (Myneni et al. 2002) as monthly averages
214 for the year 2008 for each of the four vegetated land use classes. [As a result, interannual variability is not considered in this](#)
215 [simulation as we have the same LAI curve for each PFT each year. While this somewhat limits the comparability to ET](#)
216 [observations in spring it is somewhat lessened by the fact that CLM does always use the values from two months and](#)
217 [interpolates based on the date \(for instance on the 1st of April the values from March and April would have almost equal](#)
218 [weight, while on the 14th of April the April weight is clearly dominant\).](#) This LAI is increased for all plant functional types
219 by ~~about~~ 20 percent [on average \(exact change depending on PFT, more for forests, less for grassland and crops\)](#) in the
220 summer months and significantly changed from factors less than 1 to ~~about~~ 3.3 in winter-time [\(DJF average, accounting for](#)
221 [very little changes in LAI for for-needle-leaf trees in that area\) for needle-leaf](#) forests in order to account for known biases in
222 the MODIS data (Tian et al. 2004) [mostly related to snow cover and fractional land cover due to the satellite footprint.](#) The
223 stem area index (SAI) is estimated from the LAI by a slightly modified (no dead leaves for crops, constant base SAI of 10
224 percent of the maximum LAI) formulation of Lawrence and Chase (2007) and Zeng et al. (2002) to better represent
225 European tree types. Vegetation height was set to 7m for needle-leaf trees and 10m for broad-leaf trees to account for partial
226 coverage by shrubs, to 20 - 120cm for crops, and to 10 - 60 cm for grass depending on the time of the year with low values

227 in the winter months and largest values in July and August. Since we consider only one crop type, we do not specify a
228 harvest date when the plant height drops to its minimum, but assume a smooth decline between August and October.
229 For the representation of soils in CLM we use the 1:1,000,000 soil map (BUEK1000, roughly 1km resolution) provided by
230 the Federal Institute for Geosciences and Natural Resources - BGR
231 ([http://www.bgr.bund.de/DE/Themen/Boden/Informationsgrundlagen/Bodenkundliche_Karten_Datenbanken/BUEK1000/](http://www.bgr.bund.de/DE/Themen/Boden/Informationsgrundlagen/Bodenkundliche_Karten_Datenbanken/BUEK1000/buek1000_node.html)
232 [buek1000_node.html](http://www.bgr.bund.de/DE/Themen/Boden/Informationsgrundlagen/Bodenkundliche_Karten_Datenbanken/BUEK1000/buek1000_node.html)). This soil map is available for entire Germany; thus only small areas in Switzerland and France are
233 missing outside the Neckar catchment for which we assume a nearby soil class. BUEK1000 offers sand and clay percentages
234 as well as carbon content for two to seven soil horizons down to a maximum depth of 3m for each soil type. The carbon
235 content is used to infer soil color. For urban areas (modeled as bare soil, as mentioned above) a fixed soil color (class 8 in
236 CLM) was used.

237 Since soil properties may vary substantially at scales smaller than the 1km for which BUEK1000 is appropriate, which might
238 impact system dynamics (Binley et al. 1989, Herbst et al. 2006, Rawls 1983), the soil map is downscaled by artificially
239 adding variability using the conditional points method recently presented in Baroni et al. (2017) as follows:

240 (1) The BUEK1000 soil map is randomly sampled at 1995 point locations with one sample every 5 km² on average, a
241 minimum sample distance of 250 m, and at least one sample for each soil type of the original soil map which is realistic in
242 the context of how soil maps are usually created. This strategy resulted from extensive testing by minimizing the tradeoffs
243 between reproducing the main features of the original soil map and creating variability at finer resolution.

244 (2) The sample locations are used as conditional points for further interpolation. Here, texture, carbon content, and
245 depth of the first three soil horizons are extracted from the BUEK1000 resulting in variable soil depth rather than the
246 assumed unrealistic uniform soil depth. In addition, the sand content of the original map was increased by approximately
247 20% (for clay-rich areas that previously had practically no sand, less for areas that already had high sand content to avoid
248 cases with >90% sand) resulting in a slightly higher hydraulic conductivity because previous simulations yielded too shallow
249 unsaturated zones as was expected for the resolution of this simulation. The change to sand content was a direct response to
250 this issue as it fixed most of the emerging biases:-

251 (3) Experimental variograms and cross-variograms are calculated for all variables and exponential models were fitted
252 to all spatial structures.

253 (4) A texture map (sand and clay percentage) is generated using a single realization based on conditional co-simulation
254 (Gomez-Hernandez and Journé, 1993) to provide the sub-scale variability (<1 km²). Horizon depths and carbon content are,
255 however, assumed to have a smoothed spatial variability; therefore, they are interpolated based on ordinary kriging as the
256 removal of small-scale variability is not important for the depth and carbon content.

257 (5) Since ParFlow describes retention and hydraulic conductivity curves based on van-Genuchten-Mualem parameters,
258 pedotransfer functions are applied to estimate these parameters. The pedotransfer functions of Cosby et al. (1984) is used to
259 estimate saturated hydraulic conductivity based on soil texture, the one from Rawls (1983) is used to estimate soil bulk
260 density based on soil texture and organic matter and the one from Tóth et al. (2015) is used to estimate van Genuchten

261 | ~~parameters based on soil texture and bulk density. These have been used and~~ selected based on data availability,
262 | applicability of the particular approaches, and previous evaluations conducted in the area (Tietje and Hennings, 1996).

263 | In order to keep soil porosity identical between CLM and ParFlow, we replaced the porosity calculation within CLM (which
264 | uses a different pedotransfer function). The Manning's surface roughness was set to a constant value of 5.52×10^{-4} h/m^{1/3} and
265 | the specific storage to 1×10^{-3} . The chosen surface roughness value results in a realistic base flow for the local rivers without
266 | calibration. Repercussions of this choice are discussed in Chapter 6. Slopes of the main rivers are additionally smoothed to
267 | avoid artificial ponded areas.

268 | All these changes are part of the forcing files that are provided with the full dataset making it easy to reproduce our
269 | simulations (https://cera-www.dkrz.de/WDCC/ui/cersearch/entry?acronym=Neckar_VCS_v1_FORCING)

270 | In order to allow for realistic flow in the saturated zone, the 3-D geologic model of the geological survey of the state of
271 | Baden-Württemberg was used from which eleven rock types were defined for Baden-Württemberg (see Figure A14). Some
272 | characteristic features of the domain, such as middle Triassic and Jurassic karst aquifers, are not included to avoid the
273 | manifold hydrological challenges related to its modeling. While this can have significant impact on groundwater equilibrium
274 | and dynamics on the decade time scale, for the rather short time period considered here we would simply be left with a bias.

275 | For areas outside of Baden-Württemberg we extended the rock types at the boundary outwards to cover the full
276 | computational domain. Tab. 1 summarizes porosity and hydraulic conductivity used in the domain for the different
277 | stratigraphic units. ~~Since As already mentioned above,~~ karst features of limestones are not considered, ~~and~~ porosities in
278 | stratigraphic units containing limestones and crystalline rocks are set considerably higher than in nature to somewhat counter
279 | this.

280 | Not covered by the discussed data sets (not part of the soil and not large enough to be resolved in the geological map) are the
281 | large alluvial bodies filling large part of the Neckar valley throughout the domain (Riva et al., 2006). Up to 30% of the
282 | runoff takes place in the subsurface especially during periods of base flow according to a sub-catchment simulation
283 | performed for the year 2007. In that simulation we used measured precipitation and river discharge data together with the
284 | simulated evapotranspiration to calculate the water balance over a whole year. While our simulated evapotranspiration rates
285 | may be inaccurate, it is implausible that this can account for 30% of the precipitation as in this climate we are almost always
286 | energy limited and therefore ET differences are reduced to LAI differences; i.e. the water could have left the domain only
287 | through the subsurface. Thus, gravel channels are needed to account for this lateral flow. Since the valleys in the catchment
288 | are often small compared to the limited horizontal resolution of the model, we conceptualize the alluvial bodies as gravel
289 | layers underneath all river cells (cells with a mean pressure head >0.1m) and directly next to rivers (riverbanks, i.e., one grid
290 | point besides each river cell). The assumed gravel layers reach from beneath the soil down to a depth of 8m. The gravel cells
291 | are parameterized with a high hydraulic conductivity of 1 m/h, a porosity of 0.6 and van-Genuchten parameters of 2 for n
292 | and 4m^{-1} for α (residual saturation is $0.06 \text{ cm}^3/\text{cm}^3$). Our setup results in a reasonable distribution of surface and subsurface
293 | discharge at the outlet of the catchment and reasonable river – aquifer exchange fluxes. In addition to the gravel channels, we
294 | included a layer of weathered bedrock, which starts below the soil and extends down to a depth of 6m. This layer is

295 characterized by substantially larger porosity (0.4) and hydraulic conductivity (0.1 m/h) than the rock below. This layer was
296 added to enhance subsurface flow and counter the common occurrence of too shallow water levels if these features are not
297 included. Both these changes are realistic when compared to the actual morphology of the Neckar river valley. While it is
298 quite narrow in many places, there are still significant alluvial deposits everywhere except the furthest upstream region
299 (which are not considered for this anyway due to the pressure cutoff). The choice for the weathered bedrock layer is also
300 reasonable given the temperature and moisture ranges leading to imperfections in the rock layers near the surface.

301 Since we enforce no-flow boundary conditions at the subsurface domain boundaries, all water has to eventually reach the
302 surface in order to leave the domain. This happens predominantly in areas outside of the Neckar catchment, e.g. in the upper
303 Rhine valley, thus soil-moisture values in this region may be too high.

304 **4 Results**

305 In the following, we present example results of the simulated virtual-reality simulations in order to demonstrate its potential
306 for a better understanding of the dynamics in coupled terrestrial systems. We will also show that the simulations quite well
307 resemble observations in the real Neckar catchment, and thus can be used to develop and evaluate modelling and prediction
308 strategies. Precipitation is the strongest hydrological driver in this region; thus its realistic spatial and temporal variability in
309 the domain including its statistical relations with topography is important. Also, the state of the atmospheric boundary layer,
310 which reflects the interaction of the land surface with the atmosphere is a critical component of the terrestrial system, which
311 should be represented by the simulation with some confidence. Along with the comparisons we will also discuss the
312 challenges experienced with such a modeling setup.

313 Even though we do not aim to be as close to reality as possible, we feel it important to show that the model system is
314 behaving as expected and is thus suitable for the various use cases we discussed. Figure A2 Figure 5 shows as an example
315 result a snapshot of the simulated three-dimensional distribution of cloud water/ice, precipitation density, and volumetric soil
316 moisture. The soil exhibits different soil moisture layers, the variability of which is mainly connected to different soil
317 hydraulic properties. Only clouds reaching high enough to have sufficient cloud ice produce precipitation, and some
318 precipitation evaporates before it reaches the ground. Extended weather fronts moving through the domain (not shown),
319 which are imposed by the boundary conditions, are also simulated realistically (timing, strength of wind gusts, change of
320 wind direction, change in temperature and pressure) given the resolution of the atmospheric model.

321 **4.1 Relation between water table depth and evapotranspiration**

322 An important measure for hydro-meteorological interactions within a catchment is the relation between water availability
323 and surface energy flux partitioning. Thus, the simulated catchment simulation should capture the expected reduced
324 evapotranspiration (ET) with increasing distance to groundwater (e.g., Maxwell et al., 2007; Shrestha et al., 2014). In Figure
325 3, we show daily averaged evaporation (which here is equal to ET as all other contributors are zero) values over bare soil

326 against distance to groundwater for 30th April and 31st July for the year 2007. These days were chosen as they were preceded
327 with several dry days in almost the whole catchment leading to comparable states for the upper soil layers. April was almost
328 completely dry (on average less than 3 mm precipitation over the domain), while July was much wetter, but the increased
329 solar radiation and thus temperatures compared to April result in higher evaporation rates and thus a quicker drying of the
330 top layer of the soil. Figure 3 indicates a reduction in evaporation when the distance to groundwater falls below 15 – 100cm,
331 depending on soil properties with faster evaporation reduction for increasing soil sand contents. Such relations are less
332 obvious for cells with significant plant cover: while trees show overall higher evaporation and almost no change with
333 distance to groundwater due to their deep root zones, variability increases with larger distances to groundwater (not shown).
334 Also crops and grassland show limited evaporation changes as a function of distance to groundwater, which can, however,
335 be explained by the high water availability (no water stress) in the time period considered. Figure 3 also contains a small
336 number of grid-points at water table depth of 7m or deeper with evaporation rates only slightly lower than in the shallow
337 water table regions. These relate most likely to cells that retain high levels of upper-level soil moisture even during dry
338 periods to support higher evaporation. This could be due to the way the water-table is calculated. We define the water-table
339 as the deepest threshold between positive and negative pressure. Since there are some places where there is another
340 saturated region closer to the surface, leading to higher water availability near the surface, the high value for water-table can
341 be misleading with respect to near-surface soil moisture. Such a feature will only occur if the water-table is deep enough to
342 begin with which is why we do not see this for water-tables of less than 10m. As a results volumetric soil moisture for these
343 cells with deep water table but high evaporation is much more similar to cells with shallow water table than to cells with
344 deep water table but low evaporation

345 We want to point out that in this region ET is almost always limited by atmospheric demand which is why we limit his
346 analysis to bare-soil and evaporation only. Since the upper-most layers can dry quickly the resulting drop in evaporation can
347 be seen which is not the case for ET if there is an extended root zone as we have even for crop and grassland. These bare-soil
348 areas are not a feature of the real catchment and as such can not be compared to real measurements.

349 An important measure for hydro-meteorological interactions within a catchment is the relation between water availability
350 and surface energy flux partitioning. Thus, the virtual catchment simulation should capture the expected reduced
351 evapotranspiration (ET) with increasing distance to groundwater (e.g., Maxwell et al., 2007; Shrestha et al., 2014). In Figure
352 6, we show daily averaged ET (evaporation as all other contributors are zero) values over bare soil against distance to
353 groundwater for 30th April and 30th July for the year 2007. April was almost completely dry (on average less than 3 mm
354 precipitation over the domain), while July was much wetter, but the increased solar radiation and thus temperatures
355 compared to April result in higher ET rates and thus a quicker drying of the top layer of the soil. Figure 6 indicates a
356 reduction in ET when the distance to groundwater falls below 15 – 100cm, depending on soil properties with faster ET
357 reduction for increasing soil sand contents. Such relations are less obvious for cells with significant plant cover: while trees
358 show overall higher ET and almost no ET change with distance to groundwater due to their deep root zones, ET variability
359 increases with larger distances to groundwater (not shown). Also crops and grassland show limited ET changes as a function

360 of distance to groundwater, which can, however, be explained by the high water availability (no water stress) in the time
361 period considered. Figure 6 also contains a small number of grid-points at water table depth of 7m or deeper with
362 evaporation rates only slightly lower than in the shallow water table regions. These relate most likely to cells that retain high
363 levels of upper-level soil moisture even during dry periods to support higher evaporation. This could be either because of the
364 soil properties or due to high flow from neighboring cells. Time-series of soil moisture for the 10 days preceding 30th April
365 and 30th July are shown in Figure 7 to illustrate this effect. It can be seen that volumetric soil moisture for cells with deep
366 water table but high evaporation is much more similar to cells with shallow water table than to cells with deep water table
367 but low evaporation. This means that these cells can retain high upper level soil moisture despite having a low groundwater
368 level. Most of these cells are near rivers and can receive just the right amount of water from lateral flow to keep evaporation
369 high while groundwater level stays low.

370 Precipitation

371 We compare the simulated precipitation with the $1 \times 1 \text{ km}^2$ gridded REGNIE product of DWD, derived from in-situ
372 precipitation observations (Rauthe et al., 2013). For the evaluation of seasonal daily precipitation cycles hourly observations
373 of 71 DWD observational stations are used. The simulated seasonal mean precipitation (Figure 58) and the annual mean
374 precipitation (not shown) are governed by the orographic structures of the Black Forest and Swabian Alb. Values range
375 between approximately 520 mm/year around Mannheim and 2105 mm/year over the Black Forest in good accordance with
376 REGNIE concerning the overall pattern and range (510 mm/year – 2130 mm/year). Overall the simulation shows about 10%
377 higher annual precipitation in the east and south and about 25% lower in the north and west compared to REGNIE. During
378 winter (December to February) precipitation is dominated by advection from the west, which result in maxima over the
379 upwind and peak zones of the mountains and leeward minima. The simulated winter pattern (j) compares well with REGNIE
380 (k), but the model underestimates precipitation in the northwestern part of the catchment (l). Over the mountains a slight
381 lateral shift of this kind of precipitation pattern results in neighboring areas with under- and overestimation also found for
382 COSMO simulations coupled to its own TERRA land surface model (e.g., Dierer et al., 2009; Lindau and Simmer, 2013). In
383 fall, the difference pattern between simulations and REGNIE (i) is similar to the winter pattern, but has smaller contrasts. In
384 spring, the simulated precipitation is higher compared to REGNIE. In the summer (June to August), cloud bases are usually
385 higher and reduce the patterns caused by the luff-lee effects. Moist air extends further to the east and south and gets
386 stanchued by the alpine upland leading to enhanced precipitation there. The simulated summer precipitation pattern, which is
387 dominated by convective precipitation, resembles the REGNIE pattern but exceeds the latter by about 20% lower over large
388 parts of the catchment (Figure 48).

389 The mean seasonal diurnal precipitation cycles (Figure 59) reflect the dominating precipitation types. While observed and
390 simulated winter precipitation (Figure 5b9b) do not show a diurnal cycle, summer precipitation (Figure 5a9a) increases over
391 the afternoon reaching a maximum at about 7pm in accordance with the maximum of convective precipitation. The
392 simulations reproduce this pattern but exhibit a weak second peak between 6am and 12am while the afternoon/evening
393 increase is delayed by about two hours. The simulated daily precipitation distribution fits the observations especially in late

394 afternoon and night while it overestimates precipitation during the late morning while underestimating it in early afternoon
395 in summer. In Winter this effect is much less pronounced but still there. It is connected to convective showers that are still
396 too small and parametrized. These parametrizations were not originally designed for the km scale and have issues at this
397 resolution and start producing precipitation too early. quite well. While the simulated~~virtual~~ catchment has somewhat less
398 dry and low precipitation days than REGNIE, the number of days between 4 and 10 mm are higher than in REGNIE (not
399 shown). The simulated and observed seasonal precipitation cycles (Figure 6+0) compare very well and mean precipitation is
400 nearly identical between simulations and observations. The model reproduces the seasonal cycle of maximum daily
401 precipitation well, however with larger differences in the summer (see also Dierer et al. 2009).

402 4.2 Atmospheric State Variables and Surface Radiation

403 We compare the atmospheric boundary layer (ABL) of the simulated~~virtual~~ catchment to observations from the
404 meteorological tower at Karlsruhe Institute of Technology (KIT; Kalthoff and Vogel, 1992) and with DWD radiosonde
405 observations in Stuttgart (STG) (see Figure 13 for locations and Table A1 for details of observed quantities). To avoid a
406 biased comparison due to land-cover mismatches between the simulation due to only having one land-use type per gridcell
407 and the actual land use at the observation sites, the simulations are averaged over five-by-five atmospheric grid boxes
408 centered around the observation sites thus giving approximately the same fractional land cover in both cases.

409 The 10m mean diurnal minimum temperatures in the ~~virtual~~-catchment are between 0.5 K (January) and 2.5 K (August)
410 higher than observed (Figure 7+1, top) and are reached approximately one hour later than observed with the subsequent
411 morning temperature rise shifted accordingly. The simulated diurnal temperature maxima are on average 0.7 K lower than in
412 the observations and are reached 30 minutes later than measured. The morning temperature gradient in the simulation ranges
413 from 0.10 K/h in December to 0.31 K/h in April, which compares reasonably well with the observations (0.13/0.52 K/h in
414 January/April). The evening cooling, however, progresses too slowly and results in too high minimum temperatures. At 100
415 m above ground, diurnal maximum temperatures agree within 0.7 K while the warm bias of diurnal minimum temperatures
416 (0.9 K) is smaller than at 10m height (Figure 7+1, bottom). Also at 100 m a 1h shift between the diurnal minimum
417 temperatures and the morning temperature rise are found. In 200 m height, the simulated monthly mean diurnal cycles are
418 practically identical to the KIT observations (not shown). The temperature standard deviations (mean absolute difference
419 between daily and monthly mean profile)~~in the virtual catchment~~ are somewhat smaller than observed, in particular during
420 the afternoon for the summer half year when the reduction can be more than 20%.

421 COSMO in TerrSysMP estimates ABL heights via the bulk Richardson number criterion with a threshold of 0.22 for
422 unstable and 0.33 for stable conditions (Szintai and Kaufmann, 2008). Both seasonal and diurnal variations of the mean ABL
423 height at 0 and 12h local time agree well with the observations using the same criterion (Figure 8+2), but the simulation
424 tends to overestimate ABL heights at nighttime by up to 150 m and underestimate it at daytime by up to 200 m in March.
425 Figure 9+3 compares simulated mean vertical profiles of temperature, virtual potential temperature, and specific humidity
426 with radiosonde observations at 0 h and 12 h local time in Stuttgart (STG) including the mean differences (bias) and the

427 standard deviation of the differences. Simulations are up to 0.9 K warmer close to the surface at 0 h and up to 0.5 K colder at
428 12 h. At larger heights, the simulations are up to 0.5 K warmer depending on land cover. Specific humidity profiles at 0 h are
429 approximately 0.2 g/kg too dry close to the surface and 0.2 g/kg too wet above 1500 m. At 12 h profiles are up to 0.3 g/kg
430 too wet throughout. The simulations have smaller virtual potential temperature gradients and are thus less stable close to the
431 surface at 0 h. At 12 h, the decreasing virtual potential temperature close to the surface is not captured and tends towards a
432 more neutral instead of unstable profile at low heights.

433 At KIT (STG) the land surface receives on average 20 W/m^2 (5.3 W/m^2) more incoming shortwave radiation and 18 W/m^2 (8
434 W/m^2) less incoming longwave radiation indicating a somewhat lower cloud cover (or lower cloud optical depth) as
435 observed. At daytime (6 h – 22 h), the mean outgoing longwave radiation matches the KIT observations, while at nighttime
436 (22 h – 6 h) values are 7.2 W/m^2 larger than observed, which corresponds to a higher surface temperature of approximately
437 1.4 K.

438 Overall, the atmospheric profiles, including the ABL heights, are very close to observations during the day and at heights
439 above 10m~~compare very well with observations~~. Noteworthy differences only occur close to the surface with too high
440 nighttime temperatures (up to 2.5 K in summer) and subsequently too small morning temperature gradients. Somewhat
441 higher incoming shortwave and lower incoming longwave radiation at the surface indicate less cloud cover (or lower cloud
442 optical depths) compared to the observations. These results are in line with a previous evaluation of a 2.2 km COSMO
443 simulation (Ban et al. 2014). In addition, we note somewhat reduced unstable conditions at daytime close to the surface in
444 the simulations.

445 4.3 Passive Microwave Observations

446 The most direct area-covering observations of soil moisture are currently provided by L-Band (1.4 GHz) passive microwave
447 observations from satellites. The Community Microwave Emission Model (CMEM) is used as a forward operator to simulate
448 the brightness temperatures (TB) at this frequency in vertical and horizontal polarization (de Rosnay et al., 2009). CMEM
449 simulates brightness temperatures at the top of the atmosphere resulting from microwave emission and interaction by soil,
450 vegetation, and atmosphere based on the state variables of the simulated~~virtual~~ catchment. Input to CMEM are the
451 percentages of clay and sand in the soil, the coverage with open water surfaces, the profiles of soil moisture and soil
452 temperature, vegetation types, and leaf area index (LAI). Satellite orbit geometry, antenna pattern, foot-print and incidence
453 angle are taken into account following the ESA SMOS (Soil Moisture Ocean Salinity) instrument specifications, i.e. a full-
454 width-half-maximum field of view leading to a footprint of 40km across-orbit and 47km along-orbit at multiple incidence
455 angles (Kerr 2001) is applied. This antenna pattern weighs the grid-cell simulated brightness temperatures (Figure 11+4, left)
456 in order to obtain simulated~~virtual~~ SMOS observations. Finally, these synthetic observations are rendered according to pixels
457 based on the Icosahedral Snyder Equal Area (ISEA) projection at a spatial separation of about 15 km similar to the SMOS
458 LIC TB data product (Figure A4+4, right), which can then be compared with ~~real~~ observations for an indirect evaluation of
459 the simulation. Every pixel corresponds to a fixed geo-location of the real SMOS LIC data product over the modeled area.

460 Optionally, the satellite observation operator in TerrSysMP is able to also replicate the NASA SMAP (Soil Moisture Active
461 Passive) radiometer (Saavedra et al., 2016) for years beyond 2015 since when SMAP data is available.

462 We evaluate the simulated brightness temperature distribution over the domain with real SMOS observations between April
463 2011 and September 2011. The ~~real~~-SMOS observations are corrected from radio-frequency interference (RFI) effects over
464 the region following Saavedra et al. (2016). Initial results with CMEM adapted parameters for surface roughness and
465 vegetation optical thickness (which needed to be increased from its standard values found in the literature), lead to a
466 systematic underestimation of the brightness temperature of about -20K on average (see orange line in Figure ~~A3+5~~, which
467 compares real SMOS observations with the simulated brightness temperatures) and maximum and minimum differences of -
468 33K and -6K, respectively, for an incidence angle of 30°. A similar underestimation of -14K resulted for the 40° incidence
469 angle with maximum and minimum values of -34K and +15K (lower plot in Figure ~~10+6~~). Those differences are mainly
470 caused by the too large near-surface soil moisture values in the ~~simulated~~~~virtual~~ catchment. The cumulative distribution
471 functions of the satellite-derived soil moisture products and the ~~simulated~~ soil moisture ~~of the virtual catchment~~ suggests an
472 about 63% higher near-surface soil moisture compared to the satellite estimates (Saavedra et al. 2016, Figure 6) with
473 extremes of 44% and 95%. ~~With that, a~~ daily matching of the cumulative distribution functions of the ~~simulated~~~~virtual~~
474 catchment and satellite retrieved soil moisture are performed to find a factor which then is assumed to be the soil-moisture
475 bias of the simulation ~~and applied as a correction factor~~. Figure ~~10+6~~ compares true SMOS observations with simulated
476 brightness temperatures obtained without and with day-to-day correction for the assumed soil-moisture bias of the
477 simulation. The correction decreases the average bias in brightness temperature from -20K(-14K) to about -3K (-2K) for the
478 incidence angle of 30° (40°) at horizontal polarization. Similar results are found when the simulations were statistically
479 compared with observations of later years from the NASA SMAP (Fig. 3 in Saavedra et al. 2016). The remaining bias can
480 probably be further reduced by fine tuning radiation interaction parameters in CMEM, and by including orographic effects
481 on the effective incidence angle. These biases will be addressed by an improved exploitation of the uncertainty of the
482 radiation interaction parameters and by including in CMEM a two-stream approximation to better simulate cases with dense
483 vegetation in the future.

484 The microwave observations retrieved from the ~~simulated~~~~virtual~~ catchment show a typical situation encountered in data
485 assimilation; more often than not there are biases between simulated and remote sensing observations. This discrepancy
486 usually has multiple causes, which can relate to the observations themselves, assumptions in the observation operator used to
487 simulate the ~~virtual~~-observations, and in the model used to generate the systems state variables entering the observation
488 operator. Even if these differences cannot be removed, such observations can be highly valuable for data assimilation as long
489 as temporal tendencies are meaningful information. Usually, the bias is statistically corrected and thus only the information
490 in the temporal and (if meaningful) spatial variability of the observations is exploited for moving the model states towards
491 the true states.

492 4.4 Evaluation of River Discharge

493 We compare river discharge in the ~~simulated~~~~virtual~~ catchment with observations made in the Neckar catchment at the gaging
494 stations Rockenau, Lauffen, and Plochingen for a three-year period from 2007 to 2009 (Figure 11+6). The range of the
495 hydrological response to precipitation in the ~~simulated~~~~virtual~~ catchment is ~~similar to the observations showing the same~~
496 ~~responses to rain events as well as similar behavior during dry periods, which in adequate agreement with the observations;~~
497 ~~this~~ is noteworthy since no calibration to runoff data has been applied to the model. The simulated discharge peaks are,
498 however, higher and delayed by ~~about~~ one to three days compared to the observations. A reason could be a too large
499 Manning's coefficient and the model resolution. In the discussion we suggest a scaling of Mannings coefficient to account
500 for the mismatch between true river width and the model resolution in order to better represent realistic flood dynamics. In
501 spring and summer, the response to precipitation is significantly smoother than observed and peak amplitudes vary with
502 respect to peak amplitudes of the observations. The differences between observed and simulated precipitation discussed
503 above and the effects of the less predictable convective events during these seasons may also play a significant role.
504 Convective events will ~~often~~~~always~~ be displaced in space and time compared to the observations and may even show
505 different individual life cycles including lifetime and amplitude. Finally, the base flow is much lower compared to the real
506 catchment during dry periods, most likely because the grid resolution is considerably larger than the actual river width and
507 the unresolved subsurface spatial heterogeneity. An increased hydraulic conductivity via an increased soil sand content may
508 reduce the base flow further as infiltration increases.

509 The results are further evaluated comparing the flow duration curve and the monthly run off coefficient. The former
510 represents the statistical probability to exceed a specific discharge value within a given time period while the latter is the
511 ratio between runoff and precipitation over the catchment area. Figure A4+7 shows the lower exceedance probability ~~of the~~
512 ~~virtual catchment~~ compared to the observations, in particular for low discharge rates, a behavior attributed to the lower base
513 flow component and confirmed by the too low runoff coefficients in spring and summer but similar coefficients during the
514 rest of the year (Figure 12+8). We hypothesize that in this period the simulation has a lower hydrological response also due
515 to missing subsurface heterogeneity. As stated above, we have neglected karst features, which are known to produce fast
516 lateral subsurface flows.

517 Overall, the model captures the general statistical features of the catchment including the typical seasonal trends quite well,
518 while differences are noted related to hydrological extremes and base flow. These differences could be reduced by model
519 calibration from which we refrain because hydrological extremes are not primary the objective of this study. We discuss
520 options to improve the representation of river discharge further below.

521 4.5 Groundwater

522 A plausibility check of the groundwater levels is performed in two steps. First, we visually inspect the groundwater depth
523 map, shown in Figure 13a+9a. Accordingly, the model shows a ~~reasonable split~~~~good distribution~~ between shallower and

524 deeper (5 meter and below) groundwater tables compared to expected values from observations with shallower levels
525 overall. Furthermore, the deeper sections are found in the mountainous areas of the model domain, which corresponds well
526 with the real situation. It has to be noted though that regions with shallow groundwater levels often show very small values,
527 likely not to be found in the real catchment where the unsaturated zone is usually thicker. In a second step, we compare
528 simulated hydraulic heads with available data. The environmental protection agency of the state of Baden-Württemberg
529 (Landesanstalt für Umwelt, Messungen und Naturschutz – LUBW) operates 33 continuous groundwater observation wells.
530 Comparing those point measurements to simulation results of an uncalibrated model with 400m grid resolution makes little
531 sense. Instead, we compare (1) the magnitude of the fluctuation (subtracting the yearly mean from the respective time series)
532 in the groundwater table throughout the catchment during a year (calculated as the groundwater observation minus its mean,
533 shown in Figure 13b+9b) and (2) the average trend of the groundwater in the full model (calculated after subtracting the
534 mean and scaling the fluctuations to have the same magnitude. According to Figure 13b+9e, the magnitude of the
535 groundwater fluctuations isare within similar ranges as the observations (Figure 13b+9b), while a few real-observation wells
536 show larger magnitudes. Also, the fluctuations-the trends overall follow similar long-term patterns over the year (Figure
537 13cpatterns (Figure 19e). Hence, the groundwater, given the coarse resolution of the model in comparison with the compared
538 point measurements, shows a reasonable behavior.

539 5 Discussion

540 The size of the catchment and resolution considered (400 m) pose an enormous challenge in terms of required CPU-time.
541 Still, the applicability of Darcy's law with laboratory-based parameters can be debated as we have to resort to apparent
542 model parameters to produce realistic mass fluxes in the compartments. By compromising these technical and physical
543 aspects in the setup of the simulatedvirtual catchment, we experienced several challenges; threefour of them will be
544 discussed which we believe to be inherent to simulating energy and mass fluxes across compartment boundaries with partial-
545 differential-equation-based, high-resolution coupled models.

546 **Representation of rivers and surface roughness:** River flow in the ParFlow module of TerrSysMP is simulated by an
547 overland flow module. Overland flow appears when hydraulic heads in the top cells are above the land surface. As there is
548 no discrimination between overland flow and river flow, rivers in the simulation have the width of the grid resolution
549 whereas the real rivers may be significantly narrower. Overland flow is represented in ParFlow with the kinematic wave
550 approximation of the St. Venant equations with the surface friction parameterized by Manning's coefficient. Typical
551 Manning's coefficients when assigned to e.g. to a 400 m grid cell while in fact the river is much narrower, would result in
552 too high discharge values during rain events and far too low ones during dry periods. In both cases the always too low water
553 levels caused by the too wide rivers result in a poor representation of river-subsurface exchange. Our current choice of
554 Manning's coefficient in ParFlow ($5.52 \times 10^{-4} \text{ h/m}^{1/3}$) results in realistic average discharge throughout the year, albeit at too
555 low flow velocities. In order to compensate for this inconsistency, the Manning's coefficient could be scaled such that the

556 overland flow velocity in river cells equals the river flow velocity as proposed by Schalge et al. (2019), which improves the
557 phasing between simulated and observed discharge and the discharge peak. Similarly, the hydraulic conductivity of the
558 model top layer for river cells could be scaled in order to reduce the loss of too much surface water to the subsurface caused
559 by the too wide river cells. These issues will become even more severe when model resolutions are reduced, e.g., for
560 ensemble-based data assimilation because of the even higher demands for computing efficiency.

561 | **Coarsening of topography:** The still coarse topography of the ~~simulation~~~~virtual~~~~catchment~~ reduces the true hill slopes
562 where lateral flow on the surface and in the shallow subsurface takes place. This affects quick-flow components towards
563 rivers. As shown by Shrestha et al. (2015), coarse topography directly impacts the storage of water in the unsaturated zone
564 because drainage becomes less effective. This in turn can lead to an overestimation of latent and underestimation of sensible
565 heat flux. Additionally, coarse-resolution model runs result in delayed and stretched discharge peaks in the rivers. The
566 severity of this effect is proportional to the degree of topography smoothing, that is introduced by the coarser resolution;
567 therefore, any change in subsurface parameters such as hydraulic conductivity will depend on the degree of coarsening and
568 the location within a catchment. Especially in narrow valleys and in mountainous areas this will lead to an overestimation of
569 soil moisture, which we have not yet compensated by changing other parameters. Recently a method has been proposed to
570 improve these issues by scaling horizontal hydraulic conductivity (Foster and Maxwell, 2019).

571 **Soil parameters:** As outlined in section 2, the soil hydraulic parameters were generated based on soil maps of the real
572 Neckar catchment. According to the maps, the soils in the catchment consist mainly of clay and silt, which have rather low
573 saturated hydraulic conductivities and small air entry pressure values. In large areas of the domain, the water content in our
574 first simulations was close to saturation, even for upper soil layers, and the infiltration velocities were unrealistically low.
575 Reasons are the soil parameters, which do not capture the true soil heterogeneity; moreover, real infiltration often takes place
576 in root channels, small fractures, and other small structures. Thus, infiltration is always underpredicted by models using
577 observed soil parameters assuming homogeneity. Infiltration processes may be better captured with dual domain approaches,
578 which are, however, computationally demanding. A workaround would be to change the soil hydraulic parameters in order to
579 obtain stronger infiltration. Currently, we use an artificially increased sand percentage of the soils in order to stay consistent
580 with the concept of the pedotransfer functions used in CLM. We will also test known scaling rules (e.g., Ghanbarian et al.,
581 2015) to increase for example the saturated hydraulic conductivity for larger soil units. These rules should be applied on the
582 soil hydraulic parameters, estimated by the pedotransfer functions.

583 6 Conclusions and Outlook

584 In the present study we show the development and the data generated based on a integrated subsurface-land surface-
585 atmosphere system TSMP. Plausibility tests for the derived ~~simulated~~~~virtual~~ reality which tries to mimic the Neckar
586 catchment in southwestern Germany, show that the ~~simulated~~~~virtual~~ catchment is able to reproduce realistic behavior when
587 compared to measurements. Comparisons of simulated precipitation and ABL statistics show a very reasonable agreement

588 | with ~~real~~ observations. However, comparisons with observed passive microwave measurements by satellites shows clearly a
589 | systematic bias which is probably related to a mixture of systematic errors in the latter, assumptions in the used forward
590 | operator, parameterizations of land surface properties (soil parameters) in the simulation, and missing processes therein (e.g.,
591 | preferential flow, hill-slope processes). The analysis also shows a realistic connection between evapotranspiration and
592 | distance to groundwater in the ~~simulation~~~~virtual~~~~catchment~~, while larger deviations from reality are found for river discharge
593 | dynamics. The deficiencies could be traced to the model resolution, which limits the often much smaller river widths to
594 | multiples of the model resolution, and to the way river discharge is handled in the ParFlow component of TerrSysMP. A new
595 | parameterization scheme proposed by Schalge et al. (2019) will avoid such problems in future model simulations. The main
596 | issues we face for the upper Neckar are too high soil moisture and shallow groundwater levels. Several ideas have been
597 | proposed to improve the setup including scaling of the surface roughness and soil parameters in response to the results we
598 | obtained here. While these changes would show improvements, they are likely marginal or very specific (river discharge
599 | characteristics) and would therefore not warrant the great computational cost to re-run for such a long time. Future model
600 | developments of TerrSysMP may enable this option and it would be interesting to compare resulting datasets and quantify
601 | the simulation speed increase by using GPU compute technologies.

602 | Overall the results are encouraging regarding the viability of the ~~simulated~~~~virtual~~ reality as key input parameters to the land
603 | surface and subsurface show very good agreement with observations. For these reasons, the analysis show that the results
604 | can be used as a basis for the community for, among others, exploring feedbacks between compartments, identify in which
605 | conditions simplification of the models could be done (Baroni et al., 2019) or develop and test methods for assimilating
606 | observations across compartments . We encourage the scientific community to explore this data for the different
607 | applications. Within the study we also highlighted some limitations mainly due to the still sever technical limitation and the
608 | IT-requirements. We anticipate however that more sophisticated versions of ~~simulated catchments~~ ~~the virtual catchment~~
609 | (higher resolution, improved parameterization of sub-scale processes as discussed above) are already in progress that could
610 | be also compared to this ~~dataset~~~~virtual~~~~reality~~ in further study.

611 | Finally, we want to address the applicability and usefulness of this dataset for various studies. As indicated, this dataset can
612 | be valuable for data assimilation both for testing new methods or algorithms and as a standard set for synthetic observations
613 | to pull from. Due to the long timeseries we have covered almost any possible weather regime (with the exception of truly
614 | extreme events) which can be a great advantage as some algorithms may work well for most conditions but may show
615 | weaknesses for more specific ones (for instance CMEM and frozen soils). It also allows to investigate the impact of
616 | simplifications such as using a fixed atmospheric forcing instead of a model and thus disregarding feedback mechanisms.
617 | Next to data assimilation there are also model development and model analysis and comparison studies that can benefit from
618 | this dataset. If specific changes to the model system are made, for example testing a new cloud parametrization, all of the
619 | input files that are provided with this dataset can be used to quickly set up a working environment with known results to
620 | compare to. Here the length of the simulation is again an advantage since any development can be tested for relevant time
621 | slices. Going into detail on the analysis of this dataset with respect to compartment interactions may also be interesting. We

622 [have shown the overall behavior of the system over but we have not studied specific interesting events in detail. There is](#)
623 [certainly still much to be learned here if time is available to further analyze it. One of these topics is considering more](#)
624 [transient changes \(LAI and climate change\) rather than the more static picture we present. Lastly, this setup can also be](#)
625 [considered as a template for ensemble-based setups in the future. Right now, reduced resolutions are needed in order to](#)
626 [sufficiently run many members of such a coupled model system. As we have shown, even this higher resolved simulation](#)
627 [still shows some biases that are directly related to resolution so increasing resolution also in ensembles will be logical step in](#)
628 [the future to obtain better results. When this happens, the methods we used here to generate this simulation will be very](#)
629 [useful as well as the analysis presented here to decide how an ensemble should be set up based on the goal \(an ensemble for](#)
630 [flood forecasts would have very different focus than one for drought monitoring for example\).](#)

631

632 **7 Data Availability**

633 The presented ~~dataset~~[virtual catchment](#) is available in the CERA database of the German Climate Computing Center
634 (DKRZ: Deutsches Klimarechenzentrum GmbH) (Schalge et al., 2020) at https://doi.org/10.26050/WDC/Neckar_VCS_v1.
635 The full nine-year time series (2007-2015) for all three compartments has a size of roughly 40TB in compressed netCDF4
636 format. Nevertheless, we encourage the use of this data set for investigations on data assimilation, but also the general
637 functioning of catchments including cross-environmental interactions and predictability studies can profit from such
638 complete state evolutions of the regional Earth system.

639 The TerrSysMP model is built in a modular way and users are supposed to get the component models by themselves while
640 the coupling interface is provided through a git repository (<https://git.meteo.uni-bonn.de>). As of now, registration is required
641 to access the TerrSysMP git and wiki page.

642 Both ParFlow (<https://parflow.org/>) and CLM (<http://www.cgd.ucar.edu/tss/clm/distribution/clm3.5/>) are freely available for
643 download from their respective websites or repositories. COSMO is not available, but the DWD supplies it free of charge for
644 research purposes upon request. More information on this process can be found in the TerrSysMP wiki.

645

646 **Acknowledgements**

647 This research is funded by the Deutsche Forschungsgemeinschaft (DFG, FOR2131: "Data Assimilation for Improved
648 Characterization of Fluxes across Compartmental Interfaces"). The authors gratefully acknowledge the Gauss Centre for
649 Supercomputing e.V. (www.gauss-centre.eu) for funding this project by providing computing time through the John von
650 Neumann Institute for Computing (NIC) on the GCS Supercomputer JUQUEEN at Jülich Supercomputing Centre (JSC). We
651 thank the members of HPSC-TerrSys (http://www.hpsc-terrsys.de/hpsc-terrsys/EN/Home/home_node.html) and Klaus
652 Goergen in particular for invaluable technical support with the JUQUEEN supercomputer. Furthermore, we thank Prabhakar
653 Shresta and Mauro Sulis for their preliminary work and introduction to the TerrSysMP modeling platform. We also
654 acknowledge work done on an earlier version of this script by Jehan Rihani.

655 **References**

- 656 Alkama, R., Papa, F., Faroux, S., Douville, H., and Prigent, C.: Global off-line evaluation of the ISBA–TRIP flood model,
657 *Climate Dyn.*, 38, 1389–1412, doi:10.1007/s00382-011-1054-9, 2012.
- 658 Ashby, S.F., and Falgout R. D.: A parallel multigrid preconditioned conjugate gradient algorithm for groundwater flow
659 simulations, *Nuclear Science and Engineering*, 124(1), 145-159,1996.
- 660 Avissar, R., and Pielke, R. A.: A parameterization of heterogeneous land surfaces for atmospheric numerical models and its
661 impact on regional meteorology. *Monthly Weather Review*, 117(10), 2113-2136, doi:10.1175/1520-
662 0493(1989)117<2113:APOHLS>2.0.CO;2,1989.
- 663 Baldauf, M., Seifert, A., Foerstner, J., Majewski, D., Raschendorfer, M., and Reinhardt, T.: Operational convective-scale
664 numerical weather prediction with the COSMO model: description and sensitivities. *Monthly Weather Review*, 139(12),
665 3887-3905, doi:10.1175/MWR-D-10-05013.1,2011.
- 666 Ban, N., Schmidli, J., and Schaer, C.: Evaluation of the convection-resolving regional climate modelling approach in decade-
667 long simulations. *J. Geophys. Res. Atmos.*, 119, 7889–7907, doi:10.1002/2014JD021478,2014.
- 668 Baroni, G., Schalge, B., Rakovec, O., Kumar, R., Schüler, L., Samaniego, L., Simmer, C., Attinger, S.: A comprehensive
669 distributed hydrological modelling inter-comparison to support processes representation and data collection strategies. *Water*
670 *Resources Research*. <https://doi.org/10.1029/2018WR023941>, 2019
- 671 Baroni, G., Zink, M., Kumar, R., Samaniego, L., Attinger, S.: Effects of uncertainty in soil properties on simulated
672 hydrological states and fluxes at different spatio-temporal scales. *Hydrol. Earth Syst. Sci.* 21, 2301–2320.
673 <https://doi.org/10.5194/hess-21-2301-2017>, 2017.
- 674 Bashford, K. E., Beven, K. J., and Young, P. C.: Observational data and scale-dependent parameterizations: explorations
675 using a virtual hydrological reality. *Hydrological Processes* 16, 293–312. doi:10.1002/hyp.33,2002.
- 676 Binley, A., Elgy, J., and Beven, K.: A physically based model of heterogeneous hillslopes: 1. Runoff production. *Water*
677 *Resources Research*, 25, 1219–1226. doi:10.1029/WR025i006p01219,1989.
- 678 Chan, S., Njoku, E., and Colliander, A.: SMAP L1C Radiometer Half-Orbit 36 km EASE-Grid Brightness Temperatures.
679 Version 2. Boulder, Colorado USA: NASA National Snow and Ice Data Center Distributed Active Archive Center.
680 doi:10.5067/Y9C3Q3060AZ5,2015.
- 681 Chaney, N. W., Roundy, J. K., Herrera-Estrada, J. E., and Wood, E. F. (2015): High-resolution modeling of the spatial
682 heterogeneity of soil moisture: Applications in network design. *Water Resources Research* 51, 619–638.
683 doi:10.1002/2013WR014964,2015.
- 684 Clark, M. P., Fan, Y., Lawrence, D. M., Adam, J. C., Bolster, D., Gochis, D. J., Hooper, R. P., Kumar, M., Leung, L. R.,
685 Mackay, D. S., Maxwell, R. M., Shen, C., Swenson, S. C. and Zeng, X.: Improving the representation of hydrologic
686 processes in Earth system models. *Water Resources Research*, 51, 5929–5956. <https://doi.org/10.1002/2015WR017096>,
687 2015

688 Cosby, B. J., Hornberger, G. M., Clapp, R. B., and Ginn, T. R.: A Statistical Exploration of the Relationships of Soil
689 Moisture Characteristics to the Physical Properties of Soils. *Water Resour. Res.*, 0, 682–690.
690 doi:10.1029/WR020i006p00682,1984.

691 de Rosnay, P., Drusch, M., Boone, A., Balsamo, G., Decharme, B., Harris, P., Kerr, Y., Pellarin, T., Polcher, J., and
692 Wigneron, J. P.: AMMA Land Surface Model Intercomparison Experiment coupled to the Community Microwave Emission
693 Model: ALMIP-MEMP. *Journal Geophysical Research*, 114, D05108, doi:10.1029/2008JD010724,2009.

694 Davison, J.H., Hwang, H.-T., Sudicky, E.A., Mallia, D.V., Lin, J.C.: Full Coupling Between the Atmosphere, Surface, and
695 Subsurface for Integrated Hydrologic Simulation. *Journal of Advances in Modeling Earth Systems*.
696 <https://doi.org/10.1002/2017MS001052>, 2018

697 Dierer, S., Arpagaus, M., Seifert, A., Avgoustoglou, E., Dumitrache, R., Grazzini, F., Mercogliano, P., Milelli, M., and
698 Starosta, K.: Deficiencies in quantitative precipitation forecasts: sensitivity studies using the COSMO model.
699 *Meteorologische Zeitschrift*, 18 (6), 631-645, doi:10.1127/0941-2948/2009/0420,2009.

700 Foster, L.M., Maxwell, R.M., 2019. Sensitivity analysis of hydraulic conductivity and Manning's n parameters lead to new
701 method to scale effective hydraulic conductivity across model resolutions. *Hydrological Processes* 33, 332–349.
702 <https://doi.org/10.1002/hyp.13327>

703 Gasper, F., Goergen, K., Shrestha, P., Sulis, M., Rihani, J., Geimer, M., and Kollet, S.: Implementation and scaling of the
704 fully coupled Terrestrial Systems Modeling Platform (TerrSysMP) in a massively parallel supercomputing environment-a
705 case study on JUQUEEN (IBM Blue Gene/Q). *Geoscientific model development discussions*, 7, 3545-3573,
706 doi:10.5194/gmdd-7-3545-2014,2014.

707 Gomez-Hernandez, J., Journel J., and Journel, A. G.: Joint Sequential Simulation of MultiGaussian Fields, in Troia '92,
708 Amilcar Soares (Ed.), volume 1, pages 85-94, Kluwer Academic Publishers,1993.

709 Fatichi, S., Vivoni, E. R., Ogden, F. L., Ivanov, V. Y., Mirus, B., Gochis, D., Downer, C. W., Camporese, M., Davison, J.
710 H., Ebel, B., Jones, N., Kim, J., Mascaro, G., Niswonger, R., Restrepo, P., Rigon, R., Shen, C., Sulis, M., and Tarboton, D.:
711 An overview of current applications, challenges, and future trends in distributed process-based models in hydrology. *J.*
712 *Hydrol.* 537, 45–60. doi:10.1016/j.jhydrol.2016.03.026,2016.

713 Ghanbarian, B., Taslimitehrani, V., Dong,, G., and Pachepsky, Y. A.: Sample dimensions effect on prediction of soil water
714 retention curve and saturated hydraulic conductivity. *Journal of Hydrology*. 528,127-137,
715 doi:10.1016/j.jhydrol.2015.06.024,2015.

716 Haeffliger, V., Martin, E., Boone, A., Habets, F., David, C. H., Garambois, P.-A., Roux, H., Ricci, S., Berthon, L., Thévenin,
717 A., and Biancamaria, S.: Evaluation of Regional-Scale River Depth Simulations Using Various Routing Schemes within a
718 Hydrometeorological Modeling Framework for the Preparation of the SWOT Mission, *Journal of Hydrometeorology*,
719 16, 1821-1842, doi:10.1175/JHM-D-14-0107.1,2015.

720 Hein, A., Condon, L., Maxwell, R. M.: Evaluating the relative importance of precipitation, temperature and land-cover
721 change in the hydrologic response to extreme meteorological drought conditions over the North American High Plains.
722 Hydrology and Earth System Sciences 23, 1931–1950. <https://doi.org/10.5194/hess-23-1931-2019>, 2019

723 Hendricks Franssen, H. J., Alcolea, A., Riva, M., Bakr, M., Van der Wiel, N., Stauffer, F., and Guadagnini, A.: A
724 comparison of seven methods for the inverse modelling of groundwater flow. Application to the characterisation of well
725 catchments, *Adv. Water. Resour.*, 32 (6), 851-872, doi:10.1016/j.advwatres.2009.02.011,2009.

726 Herbst, M., Diekkrueger, B., and Vanderborght J.: Numerical experiments on the sensitivity of runoff generation to the
727 spatial variation of soil hydraulic properties. *Journal of Hydrology*, 326, 43–58. doi:10.1016/j.jhydrol.2005.10.036,2006.

728 Jones, J. E., and Woodward C. S.: Newton–Krylov-multigrid solvers for large-scale, highly heterogeneous, variably
729 saturated flow problems. *Advances in Water Resources*, 24(7), 763-774, 2001.

730 Jülich Supercomputing Centre. JUQUEEN: IBM Blue Gene/Q Supercomputer System at the Jülich Supercomputing Centre.
731 *Journal of large-scale research facilities*, 1, A1. doi:10.17815/jlsrf-1-18, 2015.

732 Kalthoff, N., and Vogel, B.: Counter-current and channelling effect under stable stratification in the area of Karlsruhe.
733 *Theor. Appl. Climatol.*, 45(2), 113-126, doi:10.1007/BF00866400,1992.

734 Kerr, Y H, Waldteufel, P, Wigneron, J P, Front, J and Berger, M: Soil moisture retrieval from space: The soil moisture and
735 ocean salinity (SMOS) mission. *IEEE Trans. Geosci. Re. Sens.*, 39(8): 1729–1735. DOI:<https://doi.org/10.1109/36.942551>,
736 2001.

737 Kollet, S. J., and Maxwell, R. M.: Integrated surface–groundwater flow modeling: A free-surface overland flow boundary
738 condition in a parallel groundwater flow model. *Advances in Water Resources*, 29(7), 945-958,
739 doi:10.1016/j.advwatres.2005.08.006,2006.

740 Kollet, S. J., Maxwell, R. M., Woodward, C. S., Smith, S., Vanderborght, J., Vereecken, H., and Simmer, C.: Proof of
741 concept of regional scale hydrologic simulations at hydrologic resolution utilizing massively parallel computer resources.
742 *Water Resources Research*, 46(4), doi:10.1029/2009WR008730,2010.

743 Kurtz, W., He, G., Kollet, S. J., Maxwell, R. M., Vereecken, H., and H. Franssen, H.-J.: TerrSysMP-PDAF version 1.0): a
744 modular high-performance data assimilation framework for an integrated land surface-subsurface model. *Geoscientific*
745 *Model Development*, 9(4), 1341-1360, doi:10.5194/gmd-9-1341-2016,2016.

746 Larsen, M. A. D., Refsgaard, J. C., Drews, M., Butts, M. B., Jensen, K. H., Christensen, J. H., and Christensen, O. B.:
747 Results from a full coupling of the HIRHAM regional climate model and the MIKE SHE hydrological model for a Danish
748 catchment, *Hydrol. Earth Syst. Sci.*, 18, 4733-4749, doi:10.5194/hess-18-4733-2014, 2014.

749 Lawrence, P. J., and Chase, T. N.: Representing a new MODIS consistent land surface in the Community Land Model (CLM
750 3.0). *J. Geophys. Res.*, 112, G01023, doi:10.1029/2006JG000168,2007.

751 Lindau, R., and Simmer C.: On correcting precipitation as simulated by the regional climate model COSMO-CLM with daily
752 rain gauge observations. *Meteorology and Atmospheric Physics*, 119, 1-2, p.31-42, doi:10.1007/s00703-012-0215-7,2013.

753 Mackay, E. B., Wilkinson, M. E., Macleod, C. J. A., Beven, K., Percy, B. J., Macklin, M. G., Quinn, P. F., Stutter, M., and
754 Haygarth, P. M.: Digital catchment observatories: A platform for engagement and knowledge exchange between catchment
755 scientists, policy makers, and local communities. *Water Resour. Res.*, 51(6), 4815-4822. doi:10.1002/2014WR016824,2015.
756 Maxwell R. M., Chow F. K., Kollet S. J.: The groundwater-land-surface-atmosphere connection: Soil moisture effects on the
757 atmospheric boundary layer in fully-coupled simulations, *Advances in Water Resour.*, 30(12), 2447-2466, 2007
758 Myneni, R. B., Hoffman, S., Knyazikhin, Y., Privette, J. L., Glassy, J., Tian, Y., Wang, Y., Song, X., Zhang, Y., Smith, G.
759 R., Lotsch, A., Friedl, M., Morisette, J. T., Votava, P., Nemani, R. R., and Running, S. W.: Global products of vegetation
760 leaf area and fraction absorbed PAR from year one of MODIS data. *Remote Sensing of Environment*, 83(1), 214-231,
761 doi:10.1016/S0034-4257(02)00074-3,2002.
762 Oleson, K. W., Niu, G. Y., Yang, Z. L., Lawrence, D. M., Thornton, P. E., Lawrence, P. J., and Qian, T.: Improvements to
763 the community land model and their impact on the hydrological cycle. *Journal of Geophysical Research: Biogeosciences*
764 (2005–2012), 113(G1), doi:10.1029/2007JG000563,2008.
765 Poltoradnev, M., Ingwersen, J., and Streck, T.: Spatial and temporal variability of soil water content in two regions of
766 Southwest Germany during a three-year observation period. *Vadose Zone Journal*, 15(6),
767 doi:10.2136/vzj2015.11.0143,2016.
768 Rauthe, M., Steiner, H., Riediger, U., Mazurkiewicz, A., and Gratzki, A. (2013): A Central European precipitation
769 climatology – Part I: Generation and validation of a high-resolution gridded daily data set (HYRAS), Vol. 22(3), p 235–256,
770 doi:10.1127/0941-2948/2013/0436,2013.
771 Rawls, W. J.: Estimating soil bulk density from particle size analysis and organic matter content. *Soil Sci.*, 135 (2), 123-
772 125,1983.
773 Ridler, M. E., van Velzen, N., Hummel, S., Sandholt, I., Falk, A. K., Heemink, A., and Madsen, H.: Data assimilation
774 framework: linking an open data assimilation library (OpenDA) to a widely adopted model interface (OpenMI), *Environ.*
775 *Modell. Softw.*, 57, 76–89, doi:10.1016/j.envsoft.2014.02.008, 2014.
776 Riva, M., Guadagnini, L., Guadagnini, A., Ptak, T., and Martac, E. (2006): Probabilistic study of well capture zones
777 distribution at the Lauswiesen field site. *J. Contam. Hydrol.* 88, 92–118, doi:10.1016/j.jconhyd.2006.06.005,2006.
778 Saavedra P., Simmer, C., and Schalge, B.: Evaluation of modeled high resolution soil moisture virtual brightness
779 temperature compared to space-borne observations for the Neckar catchment. *IEEE Xplore 14th Specialist Meeting on*
780 *Microwave Radiometry and Remote Sensing of the Environment (MicroRad)*, pp. 85-90,
781 doi:10.1109/MICRORAD.2016.7530510,2016.
782 Saavedra, P. and Simmer, C.: An Octave/MATLAB® Interface for Rapid Processing of SMOS L1C Full Polarization
783 Brightness Temperature. *Journal of Open Research Software*, 6, 1, p.2, DOI: <http://doi.org/10.5334/jors.165>, 2018
784 Schaefer, D., Dahmke, A., Kolditz, O., and Teutsch, G.: Virtual Aquifers: A Concept for Evaluation of Exploration,
785 Remediation and Monitoring Strategies. In: *Calibration and Reliability in Groundwater Modelling: A Few Steps Closer to*

786 Reality (Proceedings of the ModelCARE 2002 Conference held in Prague, Czech Republic, June 2002), edited by K. Kovar,
787 Z. Hrkal, IAHS Publication 277, IAHS Press Oxfordshire, pp. 52-59,2002.

788 Schalge, B., Haeflinger, V, Kollet, S, and Simmer, C: Improvement of surface runoff in the hydrological model ParFlow by
789 a scale-consistent river parameterization. Accepted for publication in Hydrological Processes, 2019.

790 Schalge, Bernd; Baroni, Gabriele; Haese, Barbara; Erdal, Daniel; Geppert, Gernot; Saavedra, Pablo; Haeflinger, Vincent;
791 Vereecken, Harry; Attinger, Sabine; Kunstmann, Harald; Cirpka, Olaf A.; Ament, Felix; Kollet, Stefan; Neuweiler, Insa;
792 Hendricks Franssen, Harrie-Jan; Simmer, Clemens (2020). Virtual catchment simulation based on the Neckar region. World
793 Data Center for Climate (WDCC) at DKRZ. https://doi.org/10.26050/WDCC/Neckar_VCS_v1

794 Schlueter, S., Vogel, H.-J., Ippisch, O., Bastian, P., Roth, K., Schelle, H., Durner, W., Kasteel, R., and Vanderborght, J.:
795 Virtual soils: assessment of the effects of soil structure on the hydraulic behavior of cultivated soils. *Vadose Zone Journal*
796 11, doi:10.2136/vzj2011.0174,2012.

797 Schomburg, A., Venema, V., Lindau, R., Ament, F., and Simmer, C.: A downscaling scheme for atmospheric variables to
798 drive soil–vegetation–atmosphere transfer models. *Tellus B*, 62(4), 242-258, doi:10.1111/j.1600-0889.2010.00466.x,2010.

799 Schomburg, A., Venema, V., Ament, F., and Simmer, C.: Disaggregation of screen-level variables in a numerical weather
800 prediction model with an explicit simulation of subgrid-scale land-surface heterogeneity. *Meteorology and Atmospheric*
801 *Physics*, 116(3-4), 81-94, doi:10.1007/s00703-012-0183-y,2012.

802 Semenova, O., and Beven, K.: Barriers to progress in distributed hydrological modelling: Invited commentary. *Hydrological*
803 *Processes*, 29(8), 2074–2078. <https://doi.org/10.1002/hyp.10434>

804 Shi, Y., Davis, K. J., Zhang, F., Duffy, C. J., and Yu, X.: Parameter estimation of a physically based land surface hydrologic
805 model using the ensemble Kalman filter : A synthetic experiment, *Water Resources Research*, 50(1), 706-724,
806 doi:10.1002/2013wr014070,2014.

807 Shi, Y., Davis, K. J., Zhang, F., Duffy, C. J., and Yu, X.: Parameter estimation of a physically-based land surface hydrologic
808 model using an ensemble Kalman filter: A multivariate real-data experiment, *Advances in Water Resources*, 83, 421-427,
809 doi:10.1016/j.advwatres.2015.06.009,2015.

810 Shrestha, P., Sulis, M., Masbou, M., Kollet, S., and Simmer, C.: A scale-consistent terrestrial systems modeling platform
811 based on COSMO, CLM, and ParFlow. *Monthly Weather Review*, 142(9), 3466-3483, doi:10.1175/MWR-D-14-
812 00029.1,2014.

813 Shrestha, P., Sulis, M., Simmer, C., Kollet, S.: Impacts of grid resolution on surface energy fluxes simulated with an
814 integrated surface-groundwater flow model, *Hydrol. Earth Syst. Sci.*, 19, 4317-4326, doi:10.5194/hess-19-4317-2015,2015.

815 Simmer, C., Thiele-Eich, I., Masbou, M., Amelung, W., Crewell, S., Diekkrueger, B., Ewert, F., Hendricks Franssen, H.-J.,
816 Huisman, A. J., Kemna, A., Klitzsch, N., Kollet, S., Langensiepen, M., Loehnert, U., Rahman, M., Rascher, U., Schneider,
817 K., Schween, J., Shao, Y., Shrestha, P., Stiebler, M., Sulis, M., Vanderborght, J., Vereecken, H., van der Kruk, J., Zerenner,
818 T., and Waldhoff, G.: Monitoring and Modeling the Terrestrial System from Pores to Catchments - the Transregional

819 Collaborative Research Center on Patterns in the Soil-Vegetation-Atmosphere System. *Bulletin of the American*
820 *Meteorological Society*, 96, 1765–1787. doi:10.1175/BAMS-D-13-00134.1,2015.

821 Smith, V. H., Mobbs, S. D., Burton, R. R., Hobby, M., Aoshima, F., Wulfmeyer, V., and Di Girolamo, P.: The role of
822 orography in the regeneration of convection: A case study from the convective and orographically-induced precipitation
823 study. *Meteorologische Zeitschrift*, Vol. 24, No. 1, 83–97, doi:10.1127/metz/2014/0418,2015.

824 Sulis, M., Langensiepen, M., Shrestha, P., Schickling, A., Simmer, C., and Kollet, S. J.: Evaluating the influence of plant-
825 specific physiological parameterizations on the partitioning of land surface energy fluxes. *Journal of Hydrometeorology*,
826 16(2), 517-533, doi:10.1175/JHM-D-14-0153.1,2015.

827 Szintai, B., and Kaufmann, P.: TKE as a measure of turbulence. *COSMO Newsletter* 8, 2-9,2008.

828 Tian, Y., Dickinson, R. E., Zhou, L., Zeng, X., Dai, Y., Myneni, R. B., Knyazikhin, Y., Zhang, X., Friedl, M., Yu, I., Wu,
829 W., and Shaikh, M.: Comparison of seasonal and spatial variations of leaf area index and fraction of absorbed
830 photosynthetically active radiation from Moderate Resolution Imaging Spectroradiometer (MODIS) and Common Land
831 Model. *J. Geophys. Res.*, 109, D01103, doi:10.1029/2003JD003777,2004.

832 Tietje, O., and Hennings, V.: Accuracy of the saturated hydraulic conductivity prediction by pedo-transfer functions
833 compared to the variability within FAO textural classes. *Geoderma*, 69, 71–84. doi:10.1016/0016-7061(95)00050-X,1996.

834 Tóth, B., Weynants, M., Nemes, A., Makó, A., Bilas, G., and Tóth, G.: New generation of hydraulic pedotransfer functions
835 for Europe: New hydraulic pedotransfer functions for Europe. *Eur. J. Soil Sci.*, 66, 226–238. doi:10.1111/ejss.12192,2015.

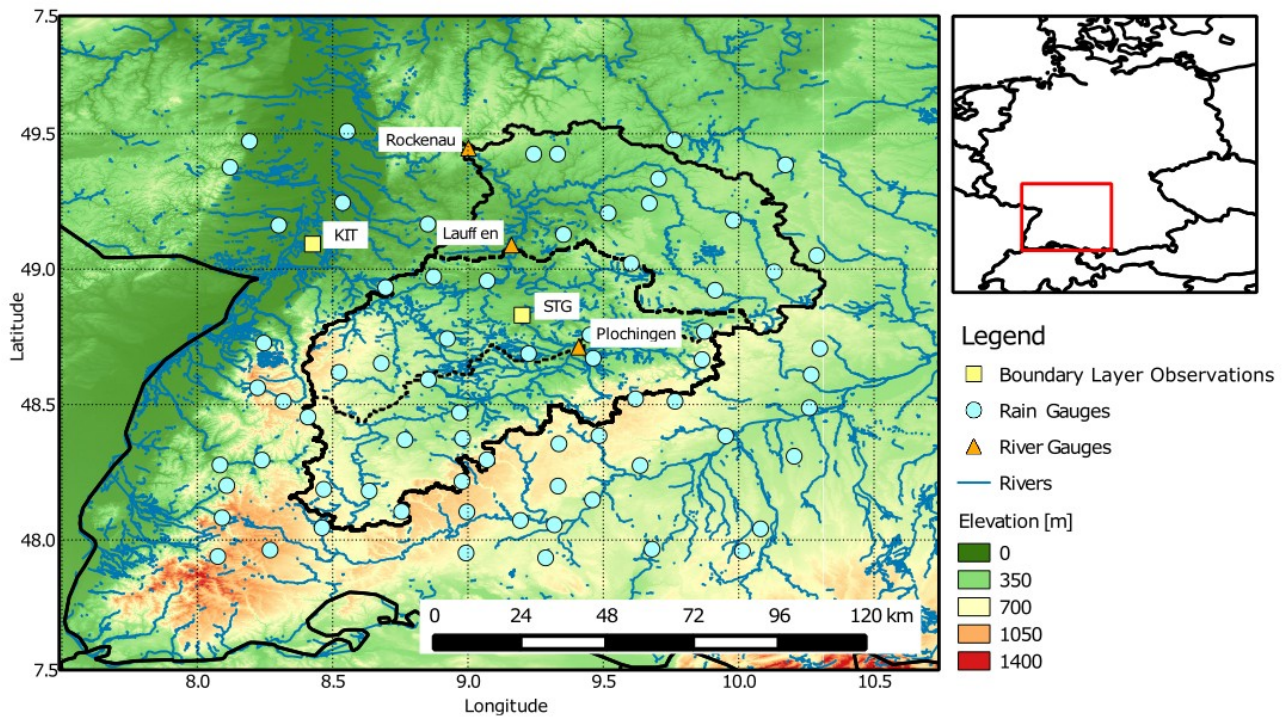
836 Valcke, S.: OASIS3 PRISM Model Interface Library: OASIS3 User Guide. PRIMS Support Initiative, Report No. 3,2006.

837 Weiler, M., and McDonnell, J.: Virtual experiments: a new approach for improving process conceptualization in hillslope
838 hydrology. *Journal of Hydrology* 285, 3–18. doi:10.1016/S0022-1694(03)00271-3,2004.

839 Zeng, X., Shaikh, M., Dai, Y., Dickinson, R. E., Myneni, R.: Coupling of the common land model to the NCAR community
840 climate model. *J. Climate* 15, 1832–1854, doi:10.1175/1520-0442(2002)015<1832:COTCLM>2.0.CO;2,2002.

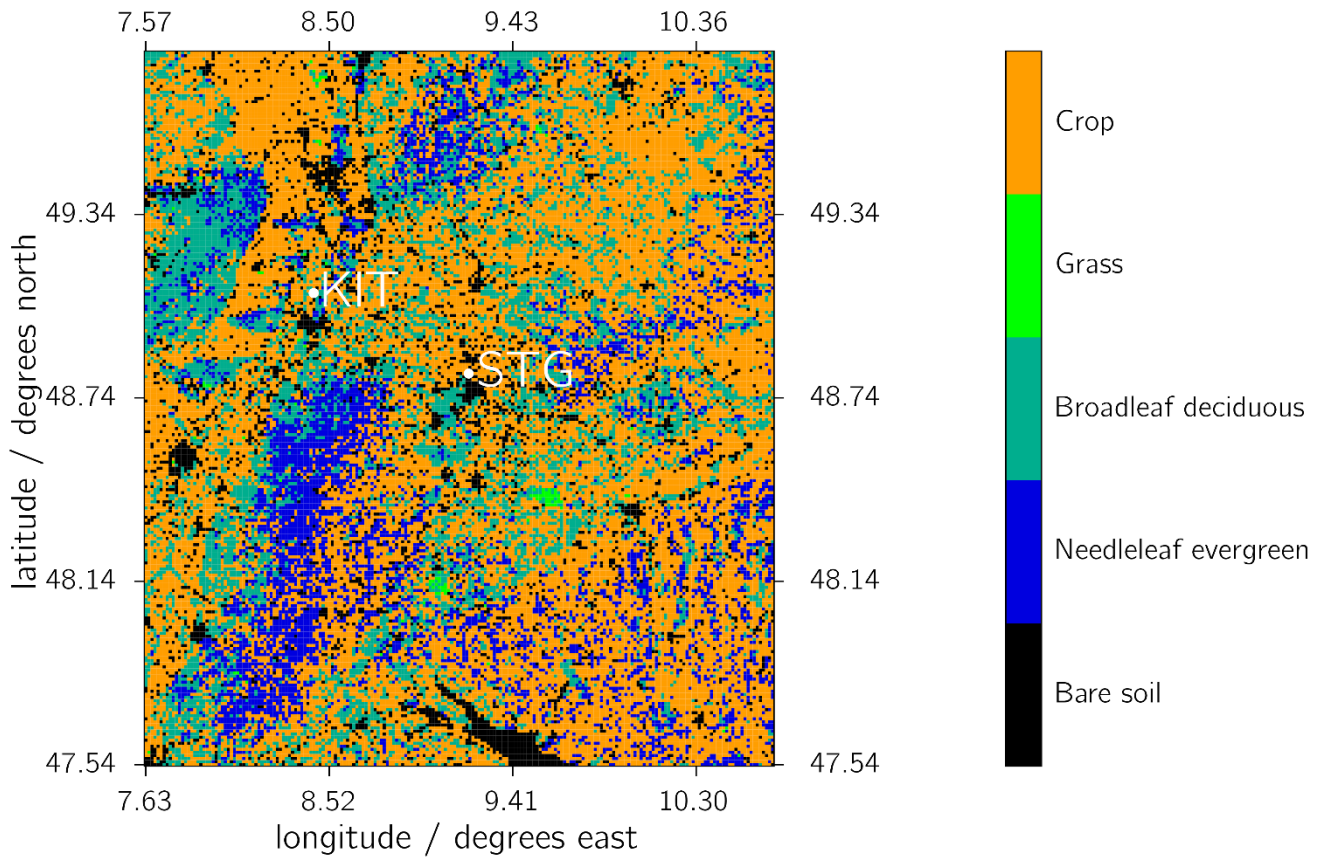
841 Zimmerman, D. A., G. de Marsily, G., C.A. Gotway, C. A., M.G. Marietta, M. G., C.L. Axness, C. L., R.L. Beauheim, R. L.,
842 Bras, R. L., Carrera, J., Dagan, G., Davies, P. B., Gallegos, D. P., Galli, A., Gomez-Hernandez, J., Grindrod, P., Gutjahr, A.
843 L., Kitanidis, P. K., Lavenue, A. M., McLaughlin, D., Neuman, S. P., RamaRao, B. S., Ravenne, C., and Rubin, Y.: A
844 comparison of seven geostatistically based inverse approaches to estimate transmissivities for modeling advective transport
845 by groundwater flow, *Water Resour Res* 34(6), 1373-1413, doi:10.1029/98WR00003,1998.

846

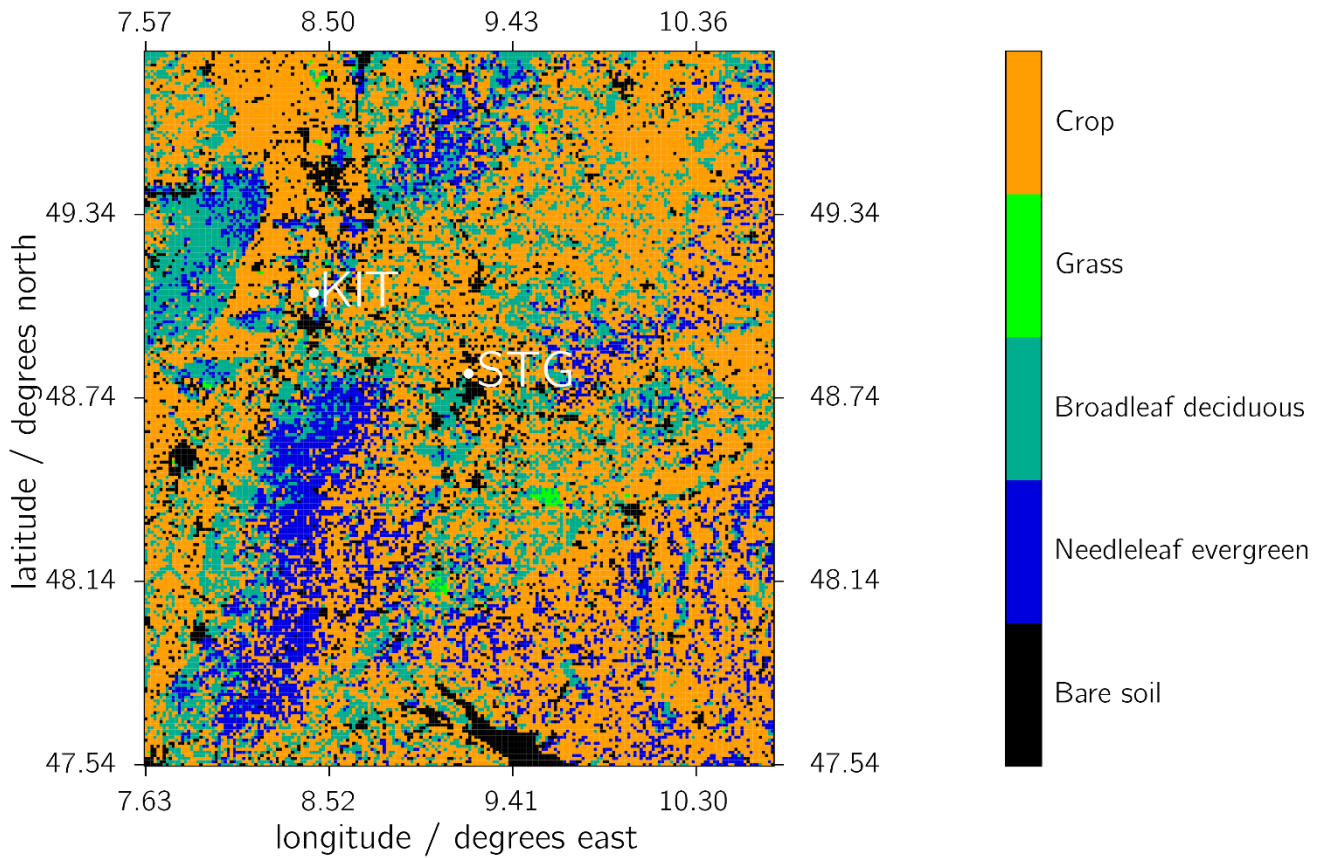


847
 848 **Figure 1: Location of the Neckar catchment within SW Germany.**

849

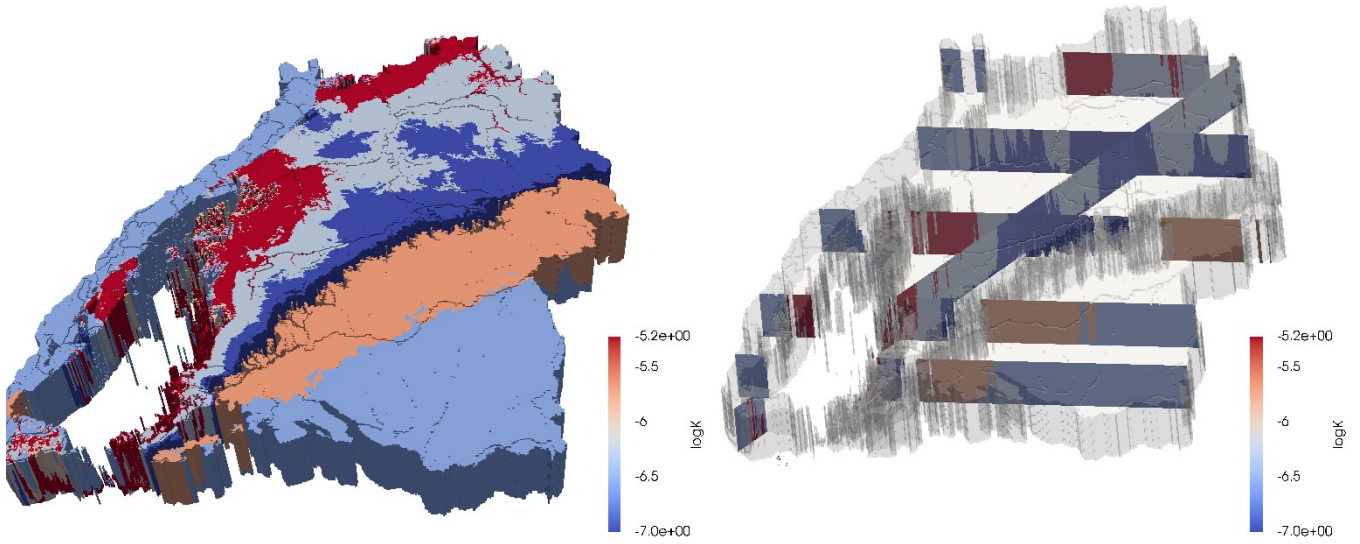


850
 851 | **Figure 2: Exchange of energy and mass fluxes in TerrSysMP (Gasper et al., 2014).**
 852 |



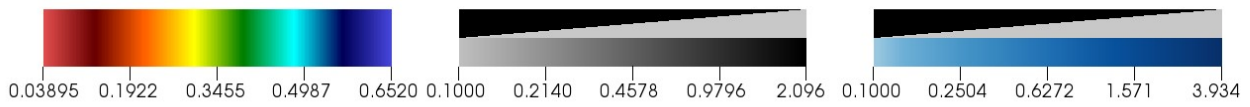
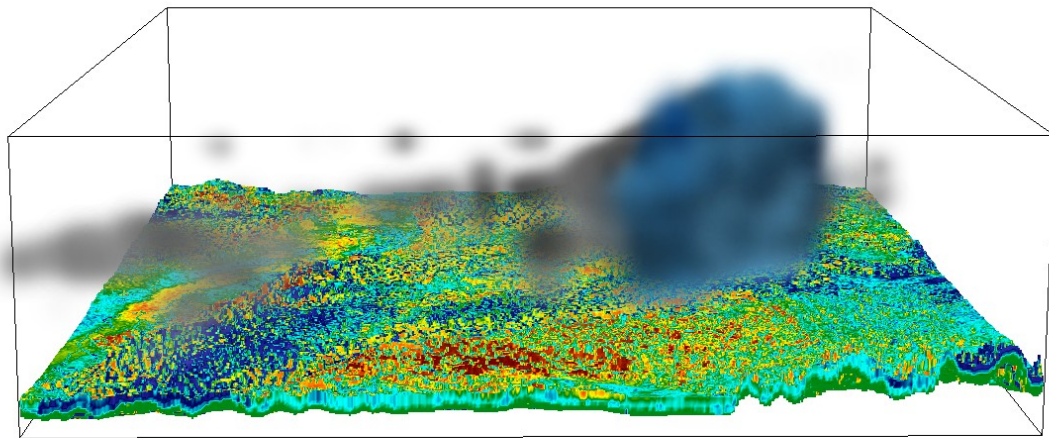
853

854 | **Figure 23:** Land cover in **the simulated domain Domain-1** covering the entire Neckar catchment and bounding areas. **KIT:**
 855 **Karlsruhe Institute of Technology** (location of meteorological tower observations), **STG:** Stuttgart (location of radiosonde
 856 **observations**).



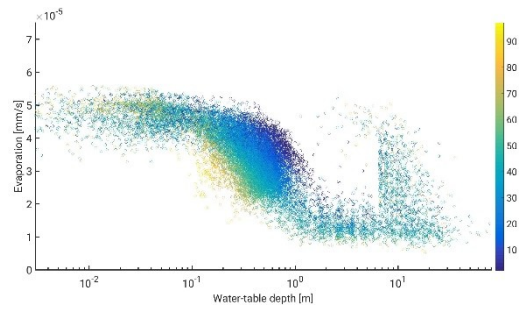
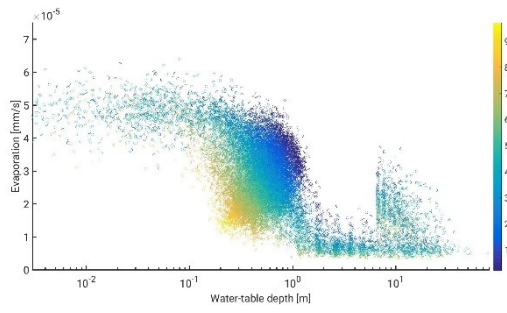
857

858 **Figure 4: Stratigraphy in the state of Baden-Württemberg represented by its logarithmic conductivity. The left figure shows a 3-D**
 859 **view of the 100 m deep geological model used in this work, where the elevation has been neglected for readability and the**
 860 **transparent regions corresponds to low-permeable material. The right figure shows the same using cross-sections to better**
 861 **visualize the vertical heterogeneity.**



862

863 **Figure 5: Snapshot of the three dimensional distribution of cloud water/ice [g/kg] (greyscale), precipitation/rain water [g/kg] (blue**
 864 **in foreground over cloud) and soil moisture [cm³/cm³] (colored) at a time point with a single rain cloud with light rain.**

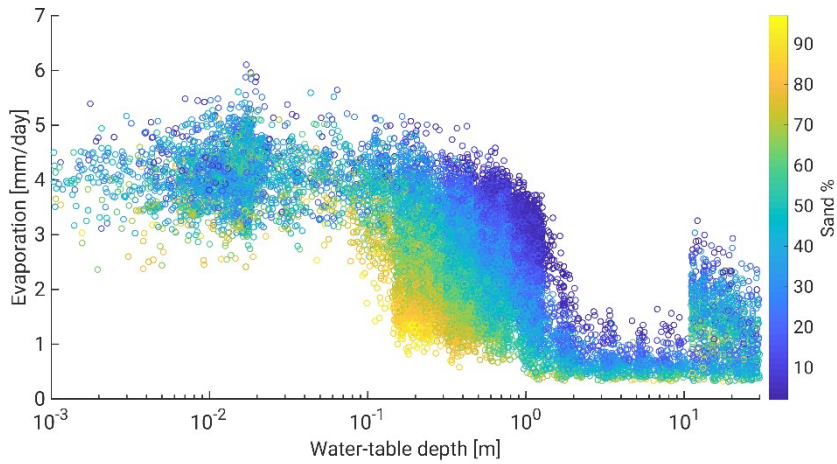


865

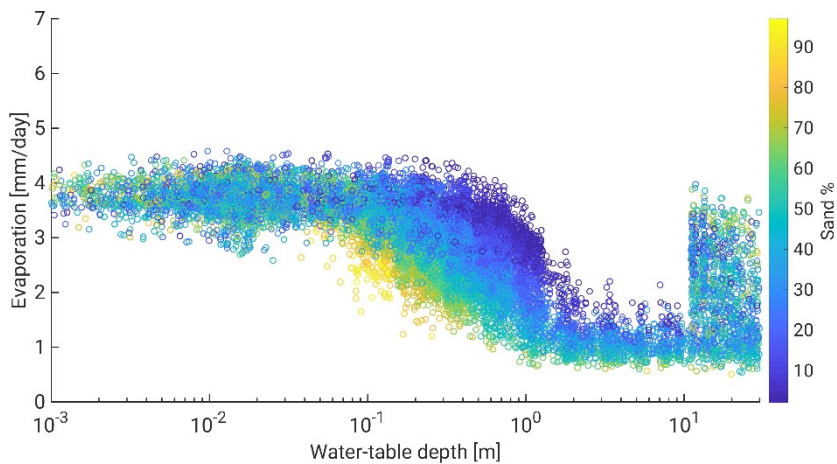
866

867

Figure 6: Daily average evapotranspiration (ET) simulated for 30th April (left) and 30th July 2007 in [mm/day]. The color indicates soil sand percentage.



868

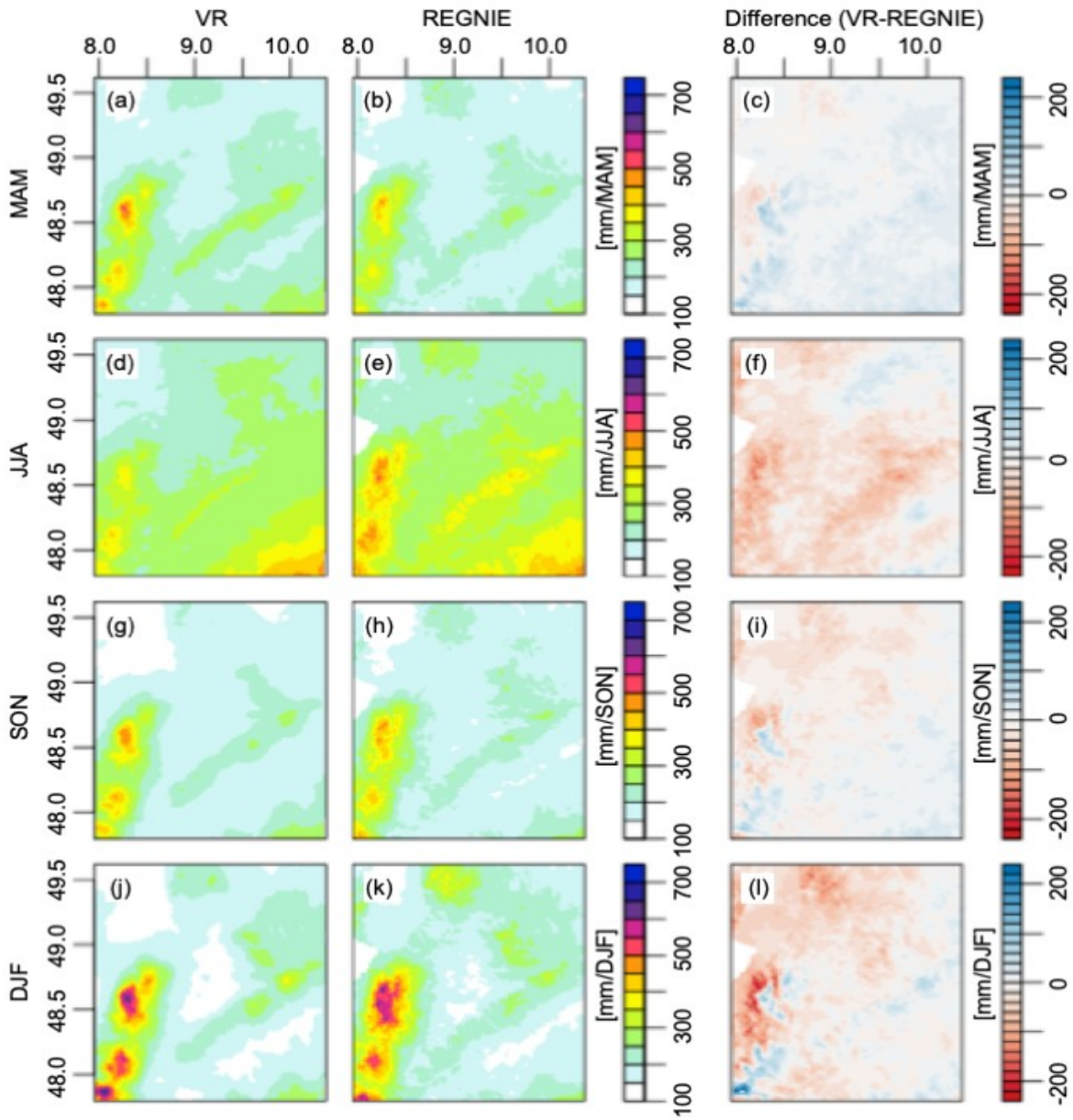


869

870 **Figure 3: Daily average evaporation simulated for 30th April (left) and 31st July 2007 in [mm/day]. The color indicates soil sand**
 871 **percentage.**

872 **Figure 7: 10-day time-series of volumetric soil moisture for three representative grid-points with high evaporation and shallow**
 873 **water-table (Shallow+High), low evaporation and deep water-table (Deep+Low), and high evaporation and deep water-table**
 874 **(Deep+High) prior to the days shown in Figure 6.**

875

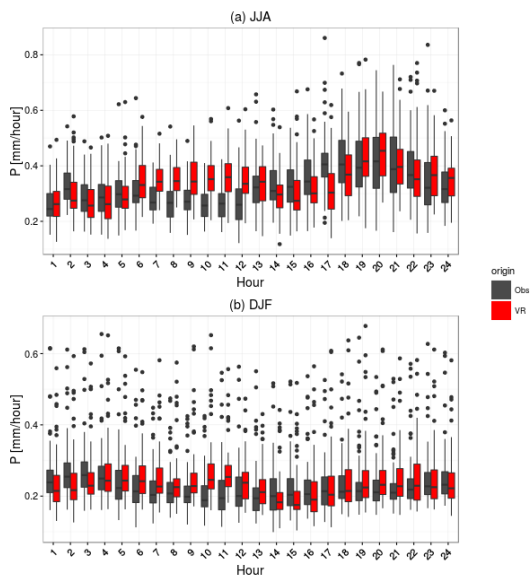


876

877 | **Figure 48:** Mean seasonal precipitation over the Neckar catchment between 2007-2013 in the **simulated virtual** reality (VR, left
 878 column) compared to the REGNIE data set (middle column). The difference between VR and REGNIE is shown in the right
 879 column. Figure (a), (b), and (c) show the comparison for spring (March – May); (d), (e), and (f) for summer (June – August); (g),
 880 (h), and (i) for fall (September – November); and (j), (k), and (l) for winter (December-February).

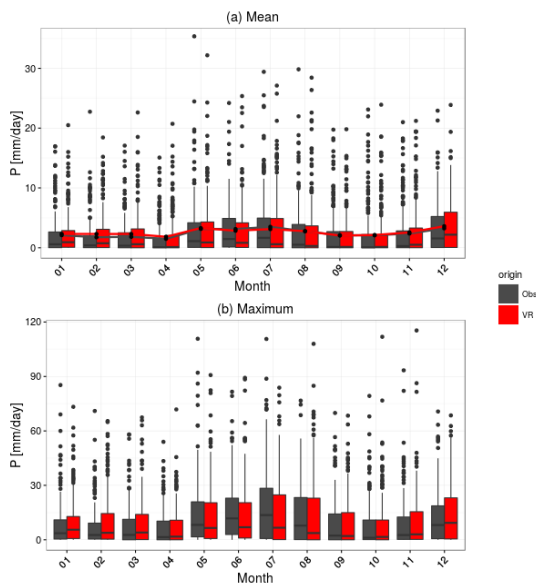
881

882



883

884 | **Figure 59:** Mean diurnal precipitation cycle for the 71 DWD stations and the corresponding simulations for wet days (more than 1
 885 [mm/day]) for June-August (a) and December-February (b) season. The upper and lower hinges correspond to the first and third
 886 quartile, the center black line the median, the upper whisker (analog for lower whisker) extends from the hinge to the highest
 887 value within 1.5*(interquartile range), and the black dots mark the outliers.



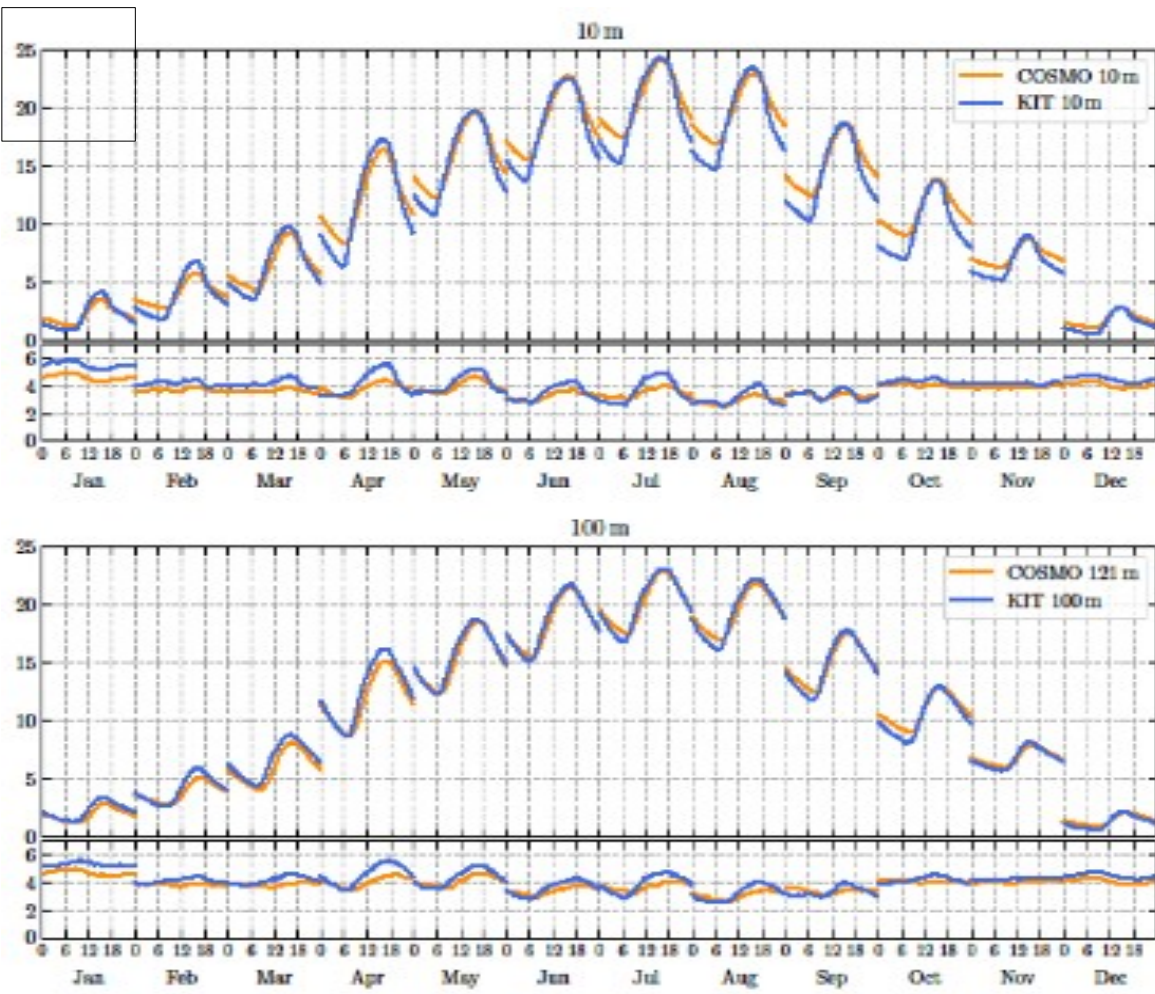
888

889

890 | **Figure 610:** (a) Daily precipitation distribution on a monthly basis as observed (black) and simulated (red). The gray and red lines
 891 indicate the monthly mean precipitation. (b) Maximum daily precipitation for the given months for the 71 DWD stations and the
 892 corresponding simulation. Box sizes as explained in the caption of Figure 10.

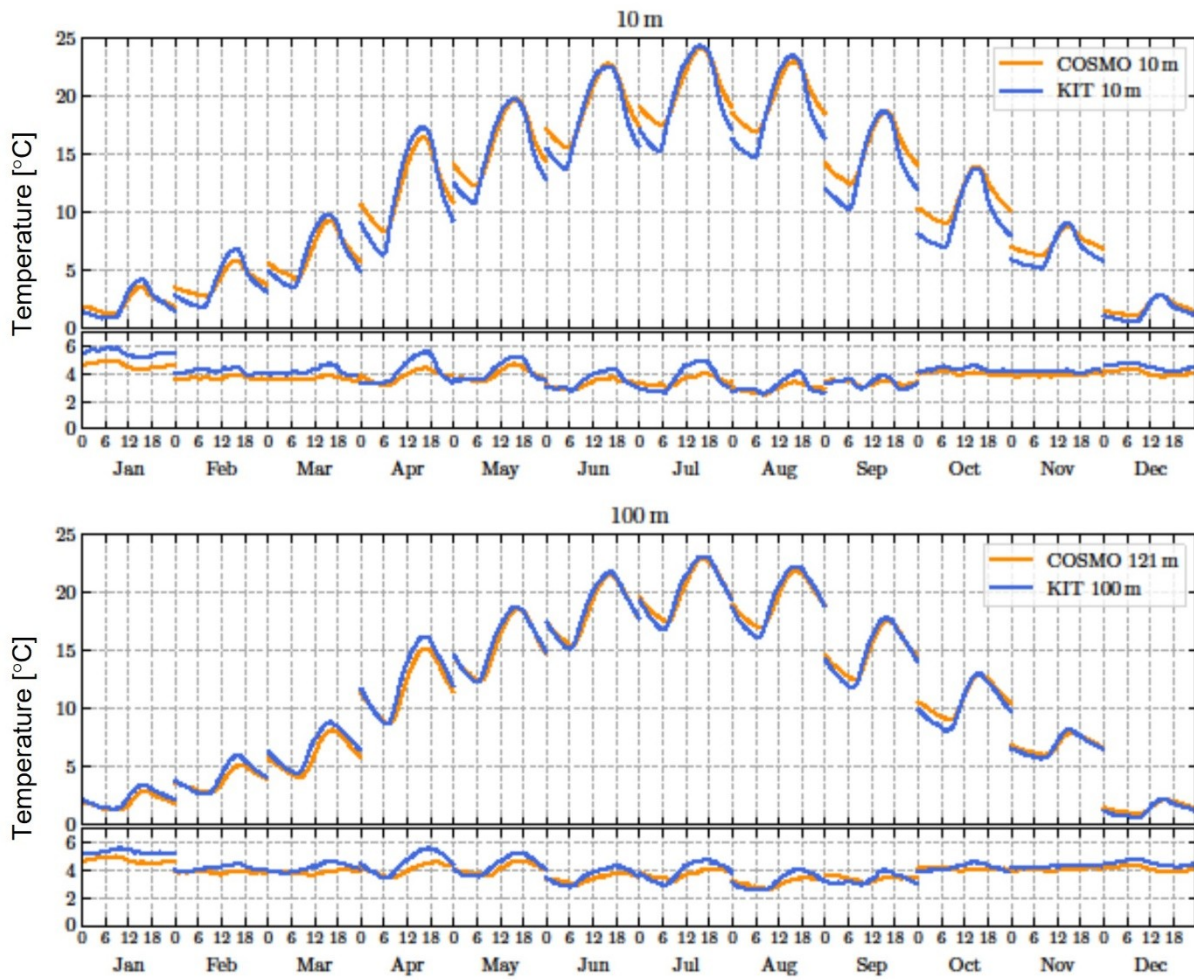
893

894



895
896
897
898

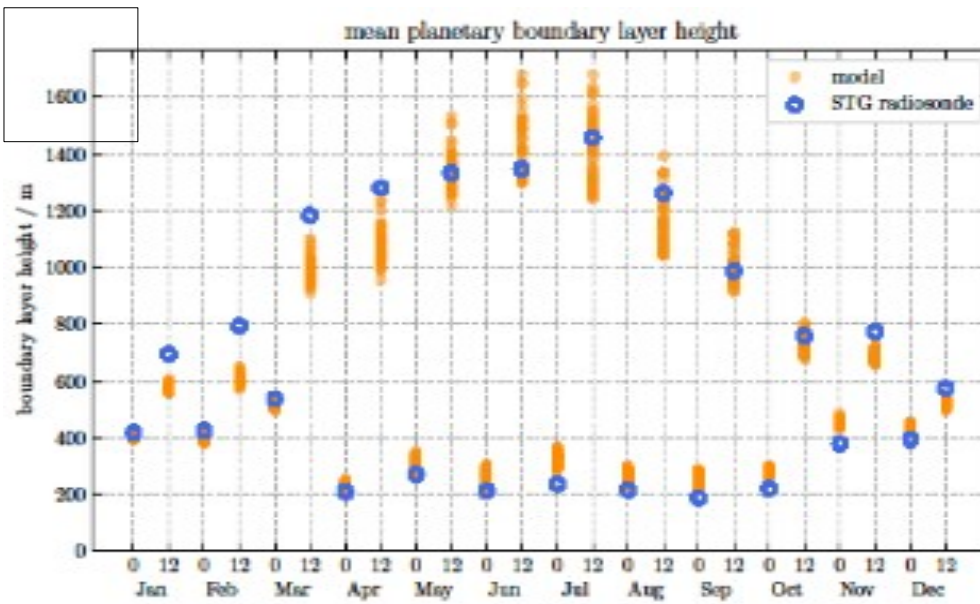
Figure 11: Monthly mean diurnal cycles (local time) and respective standard deviation for air temperature in 10-m (top) and 100-m (bottom) height at the KIT tower and for the COSMO grid boxes around the KIT location.



899

900 **Figure 7: Monthly mean diurnal cycles (local time) and respective standard deviation (see text) for air temperature [°C] in 10 m**
 901 **(top) and 100 m (bottom) height at the KIT tower and for the COSMO grid boxes around the KIT location.**

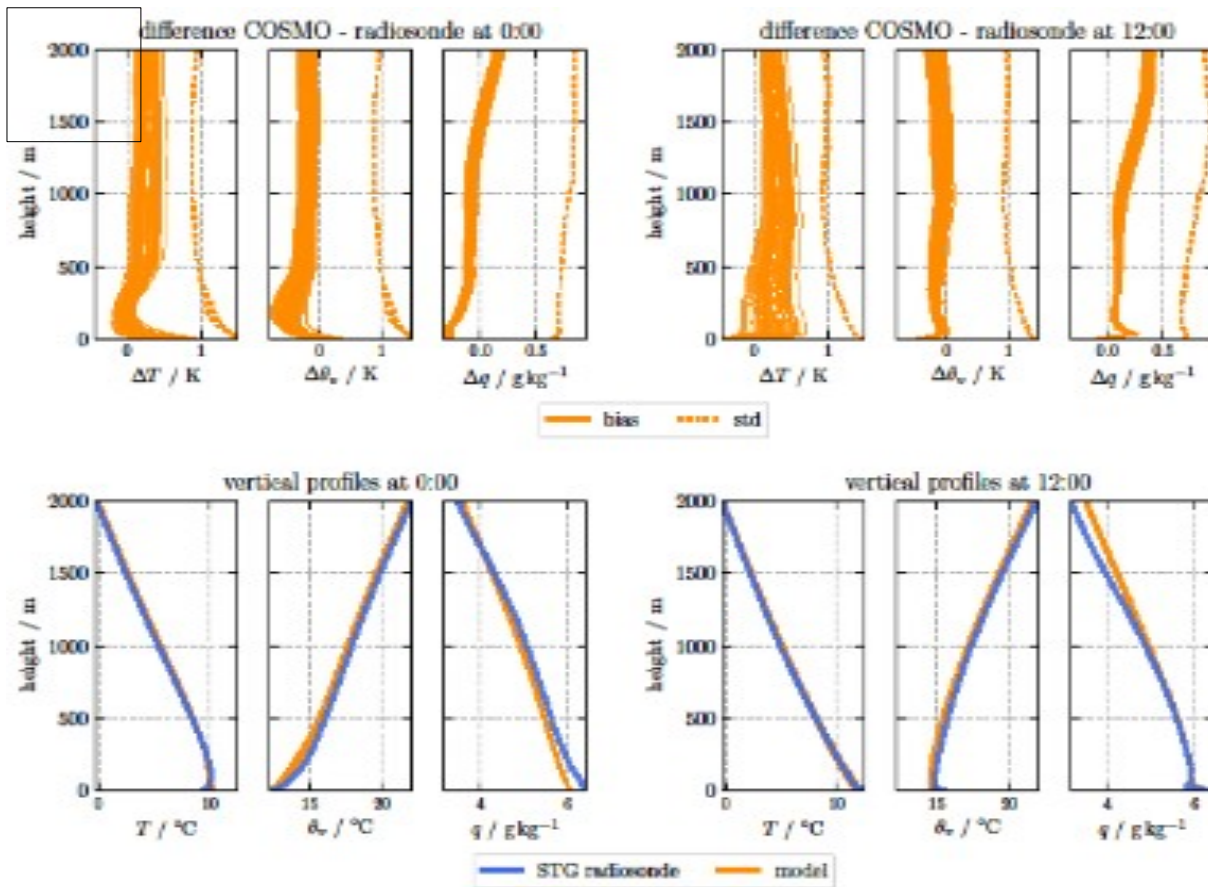
902 **Figure 12: Monthly mean boundary layer height at 0-h and 12-h local time for different land-covers diagnosed from radiosonde**
 903 **observations at Stuttgart-STG and from atmospheric profiles above grid boxes of CLM.**



904

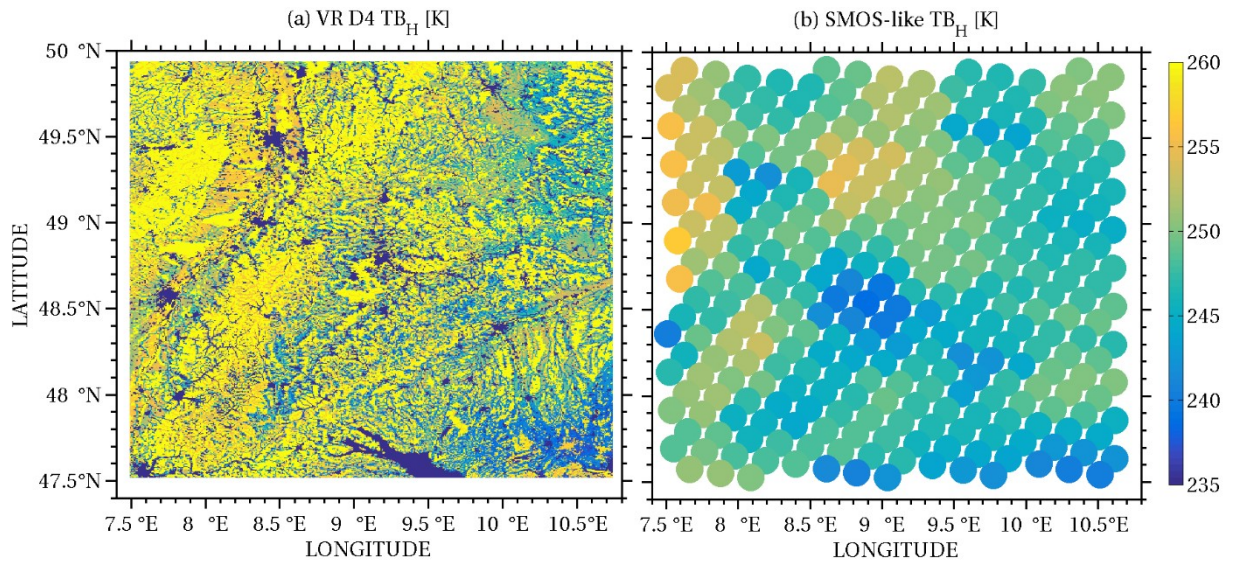
905 Figure 8: Monthly mean boundary layer height at 0 h and 12 h local time for different land covers diagnosed from radiosonde
 906 observations at Stuttgart STG and from atmospheric profiles above grid boxes of CLM.

907 Figure 13: Mean-vertical profiles of temperature, virtual-potential-temperature, and specific humidity (top), and mean-differences
 908 between modelled and observed data including the standard deviation of the differences (bottom). The experimental data are from
 909 the radiosonde data at STG and the simulated data from the grid-boxes of the virtual-catchment with different land-cover (left: 0 h
 910 local time, right: 12 h local time).

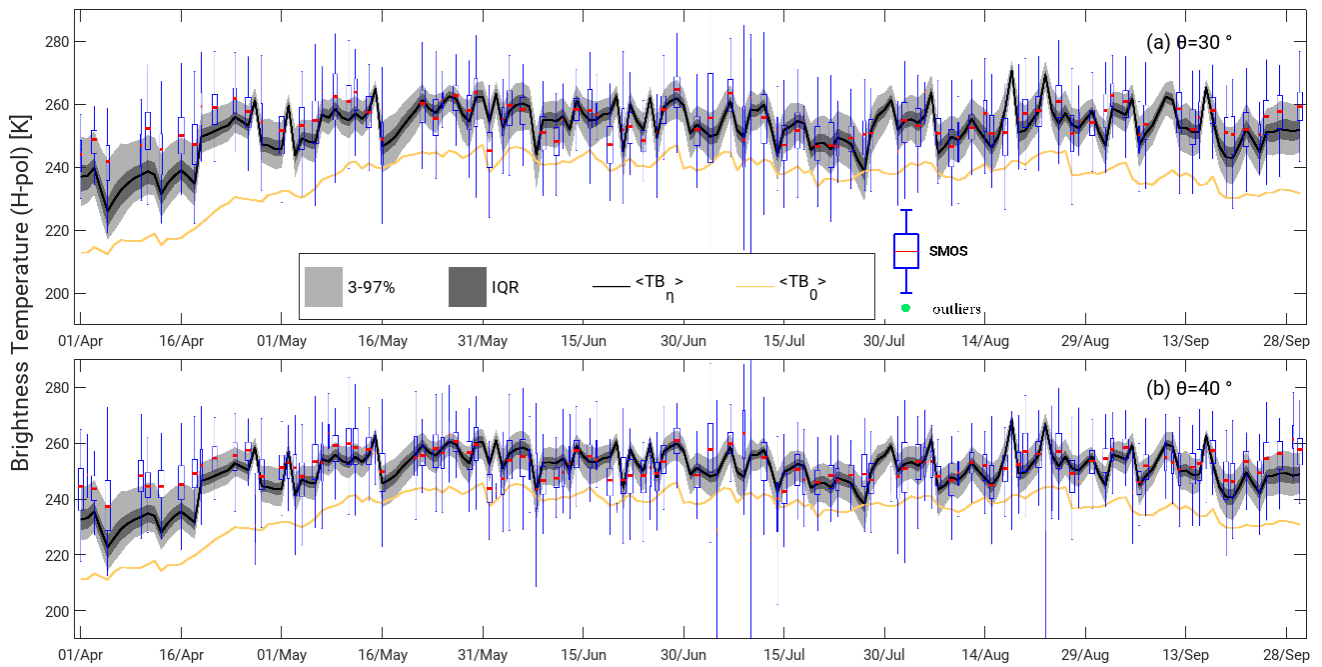


911

912 Figure 9: Mean vertical profiles of temperature, virtual potential temperature, and specific humidity (top), and mean differences
 913 between modelled and observed data including the standard deviation of the differences (bottom). The experimental data are from
 914 the radiosonde data at STG and the simulated data from the grid boxes of the simulated catchment with different land cover (left:
 915 0 h local time, right: 12 h local time).



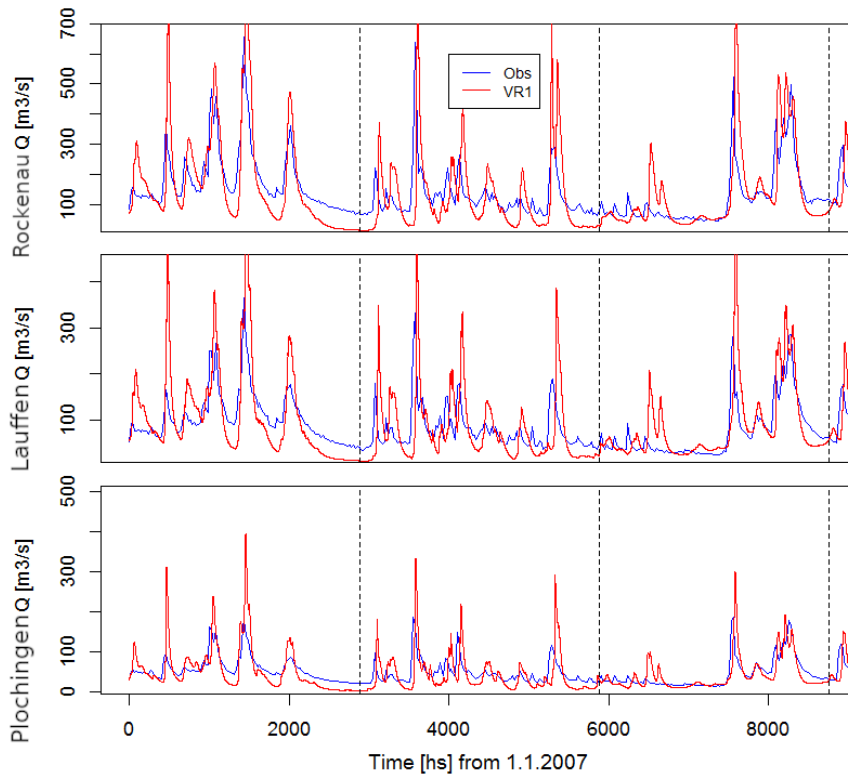
916



917

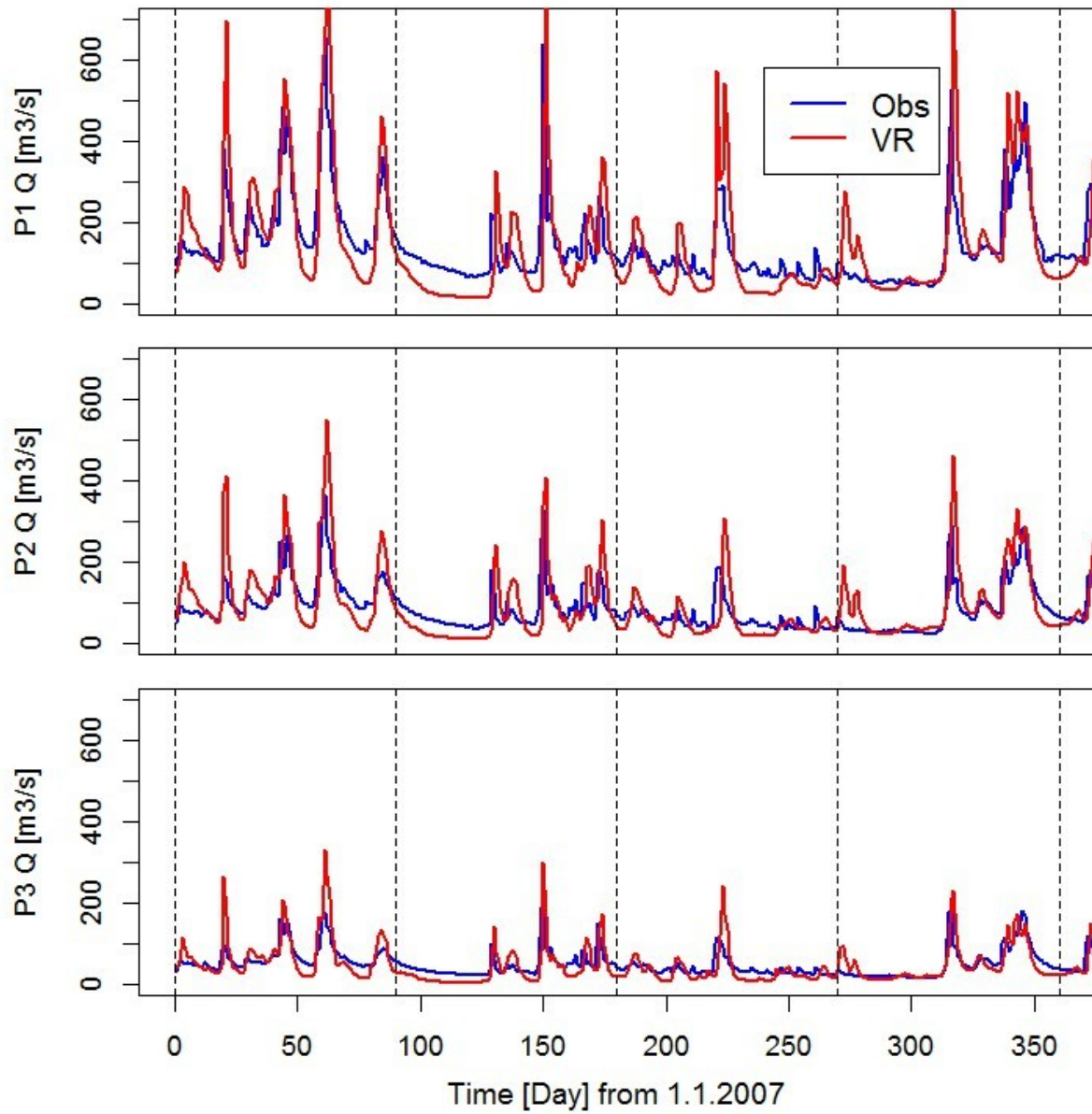
918 **Figure 10: Area-averaged L-band brightness temperature the period from April to September 2011 for an incidence angle of 30°**
 919 **(top) and 40° (bottom). The boxplots indicate the real SMOS observations averaged over the same domain. The black line is the**
 920 **median of the observations simulated with CMEM. The dark-gray area corresponds to the inter-quartile range (IQR) while the**
 921 **light-gray area encompasses the 3 to 97% range. The orange continuous line indicates the brightness temperature without taking**
 922 **into account an assumed bias in surface soil moisture content (see text).**

923 **Figure 14: Brightness temperature calculated by the application of CMEM (H-polarization) on the virtual-reality output on July**
 924 **2nd-2011 (left) and its aggregation on the spatial-resolution of the LIC data-product SMOS passive microwave radiometer (right):**



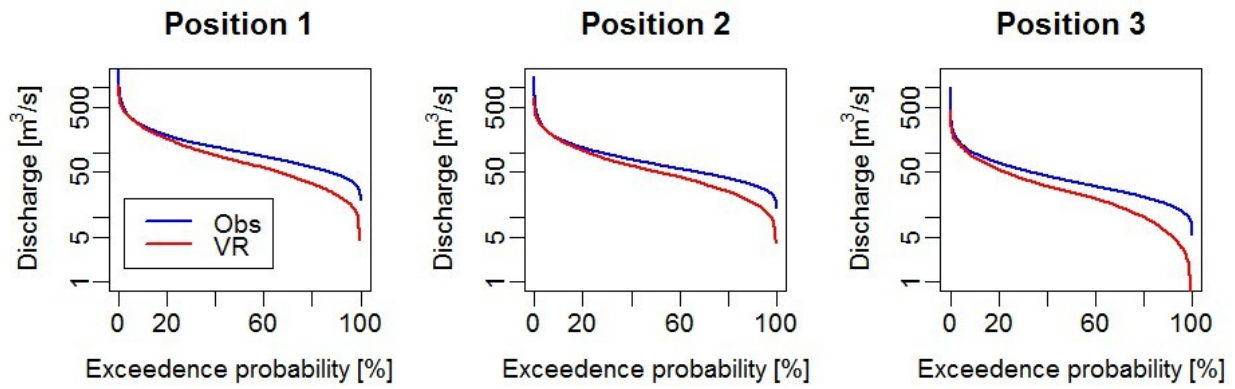
925

926 **Figure 15: Area-averaged L-band brightness temperature the period from April to September 2011 for an incidence angle of 30°**
 927 **(top) and 40° (bottom). The boxplots indicate the real SMOS observations averaged over the same domain. The black line is the**
 928 **median of the virtual observations simulated with CMEM. The dark gray area corresponds to the inter-quartile range (IQR)**
 929 **while the light gray area encompasses the 3- to 97% range. The orange continuous line indicates the brightness temperature**
 930 **without taking into account an assumed bias in surface soil moisture content (see text).**



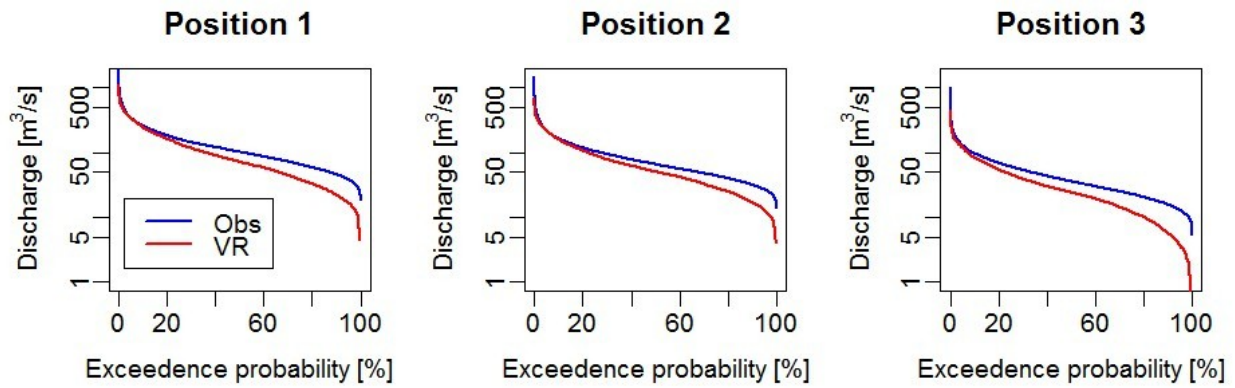
931

932 **Figure 1146:** Hourly values river discharge at the gauging stations Rockenau (P1), Lauffen (P2) and Plochingen (P3) for the year
 933 2007. Blue: observed; red: simulated virtual catchment.

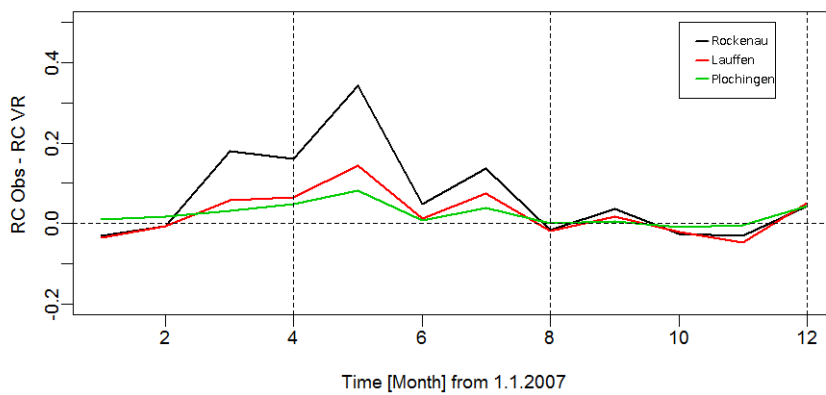


934

935 **Figure 17: Flow duration curve for the three stations for the three year time period based on. Blue: observations; red: virtual**
 936 **catchment.**

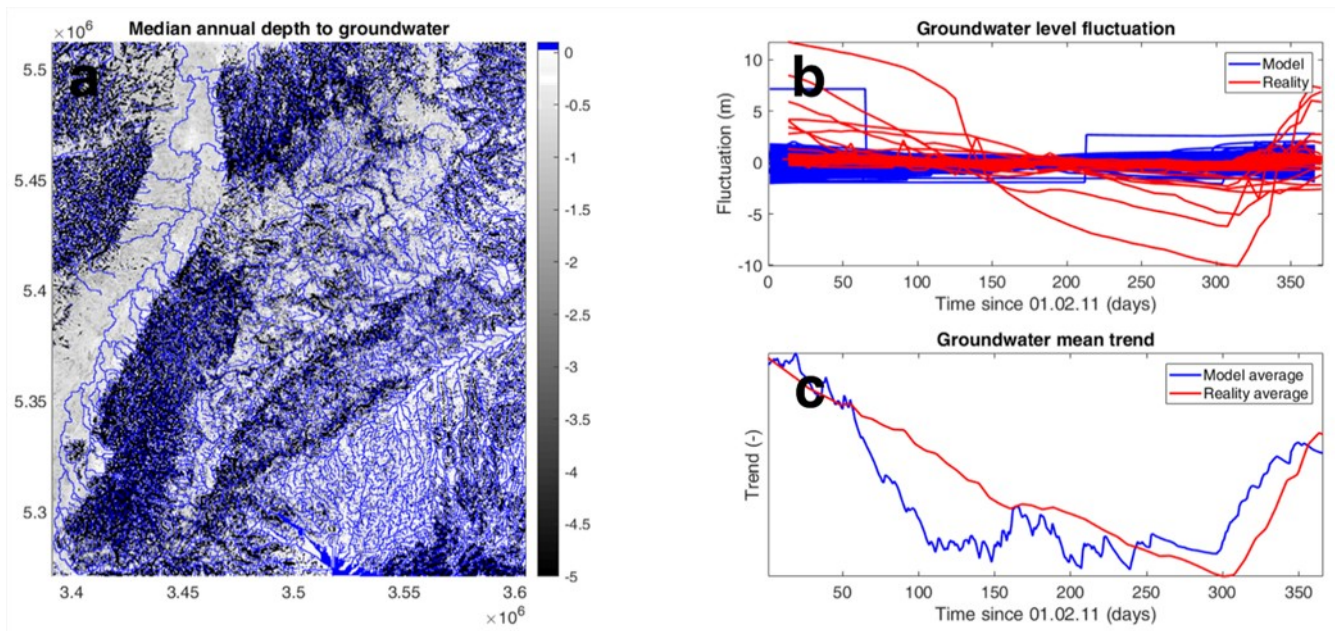


937

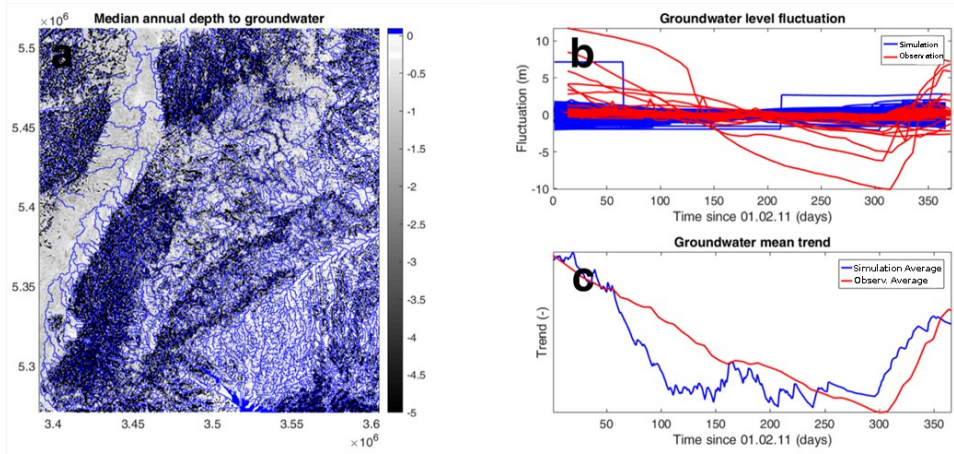


938

939 **Figure 1248:** Differences between the run off coefficient calculated for the three stations for the year 2007 based on observations
 940 and [simulation virtual catchment](#).



941



942

943 **Figure 1319:**(a) Mean groundwater table depth of the entire domain for the year ranging from 01.02.11 to 01.02.12, (b)
 944 **groundwater fluctuations around a zero mean and (c) the total mean of all model cells and all real data points superimposed on**
 945 **top of each other to show the annual average trend. Please note that for readability of the figure, subfigure (a) is limited to a**
 946 **maximum depth of -5 m, while the underlying data ranged down to -88 m**

947

948

949

950

951

952

953 **Appendix**954 **7.1 Appendix Tables**955 **Table A1: Values of porosity and hydraulic conductivity of rocks found in Baden-Wuerttemberg**

Nr.	rock type	Ksat [m/h]	porosity fraction
1	Quaternary	0.00100	0.3
2	Tertiary	0.00100	0.3
3	Upper Jura	0.00720	0.3
4	Middle Jura	10 ⁻⁷	0.3
5	Lower Jura	10 ⁻⁷	0.3
6	Upper Triassic (Keuper)	0.00036	0.3
7	Middle Triassic (Muschelkalk)	0.00180	0.3
8	Lower Triassic (Buntsandstein)	0.02160	0.4
9	Upper Permian (Rotliegendes)	0.00360	0.3
10	New Red Conglomerate	0.00100	0.3
11	Bedrock/Granite	10 ⁻⁷	0.3

956

957

958

959 **Table A2: Observed atmospheric variables at KIT and STG. Local time at STG is UTC+01.**

960

dataset	quantity	temporal resolution	height above ground	data coverage
KIT	temperature	10 min averages (resampled to 15 min)	10 m, 100 m	01/2007 – 12/2013
	Incoming and outgoing shortwave radiation		-	
	Incoming and outgoing longwave radiation		-	06/2011 – 12/2013
STG	temperature	12 h (11:45 h and 23:45 h local time)	vertical profiles (interpolated to model levels)	01/2007 – 12/2013
	dew point temperature			
	pressure			
	incoming shortwave radiation	1 h averages	-	
	incoming longwave radiation	-		

961

962

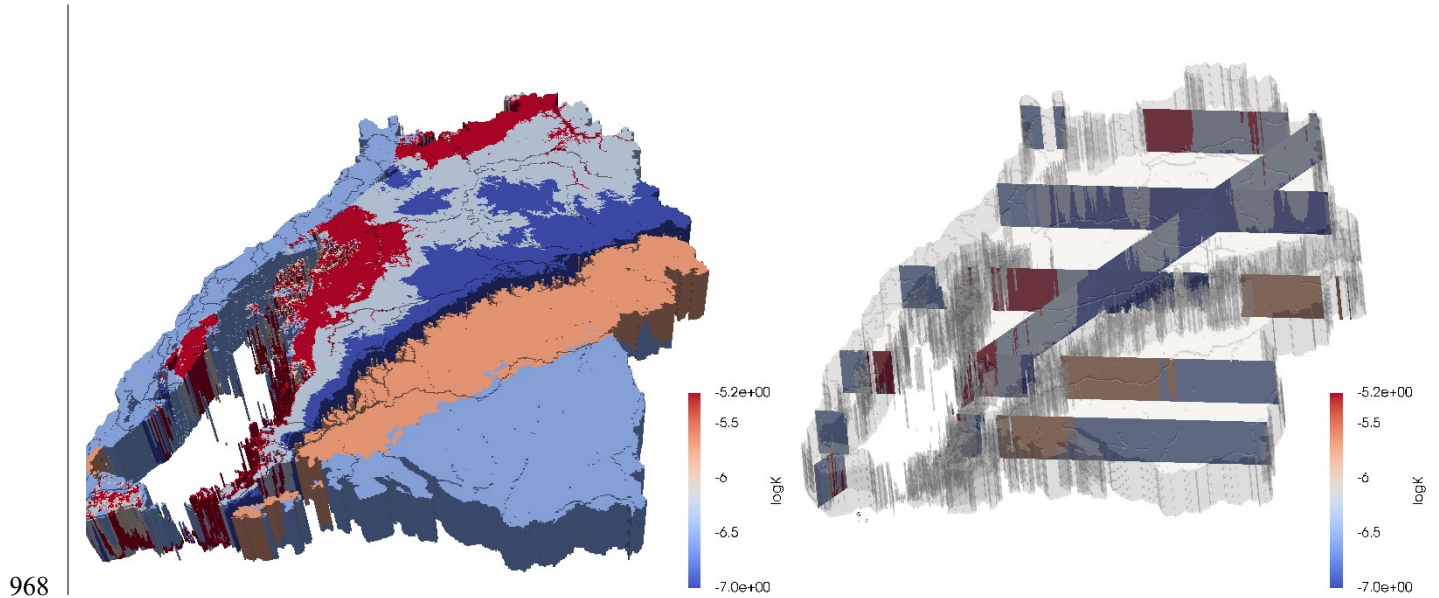
963

964 | **Table A3: Strengths and Weaknesses of our simulation regarding several variables**

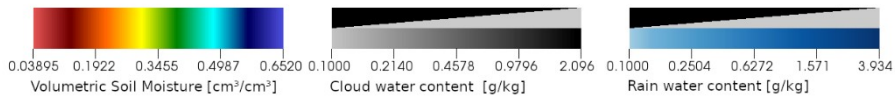
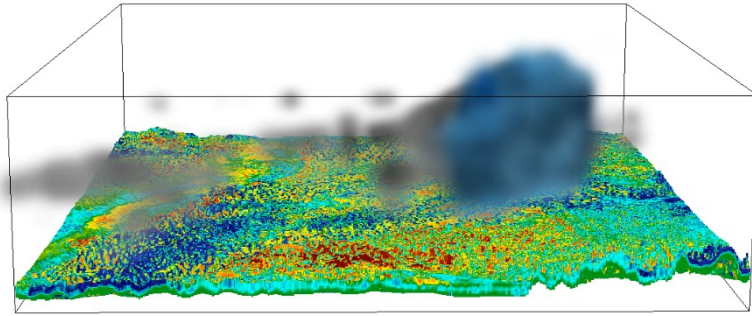
<u>Variable</u>	<u>Strength</u>	<u>Weakness</u>	<u>Other comment</u>
<u>River discharge</u>	<u>Adequately captures flood events</u>	<u>Underestimated base flow</u>	<u>Could be improved by higher resolution of the river cells (ParFlow in general)</u>
<u>ET</u>	<u>Shows expected behavior</u>	<u>Little variability in forests as they are never water limited</u>	=
<u>Precipitation</u>	<u>Good agreement with observations in general</u>	<u>Some specific areas show larger differences</u>	<u>Could be fixed by larger simulation area and new parametrizations for the 1km scale</u>
<u>ABL representation</u>	<u>Good fit to tower and radiosonde observations, especially during the daytime in summer</u>	<u>Overestimated nighttime temperature, especially in the summer</u>	<u>Related to COSMO parametrization of near surface inversion at night</u>
<u>Groundwater dynamics</u>	<u>Dynamics closely resembles measured dynamics</u>	<u>Absolute values are biased</u>	<u>Could be related to our simplification of not considering karst</u>
<u>Large-scale soil moisture (satellite)</u>	<u>Dynamics throughout the year are captured well</u>	<u>Large bias in absolute values</u>	

965 |

966 |



969 Figure A1: Stratigraphy in the state of Baden-Württemberg represented by its logarithmic conductivity. The left figure shows a 3-
970 D view of the 100 m deep geological model used in this work, where the elevation has been neglected for readability and the
971 transparent regions corresponds to low-permeable material. The right figure shows the same using cross-sections to better
972 visualize the vertical heterogeneity.

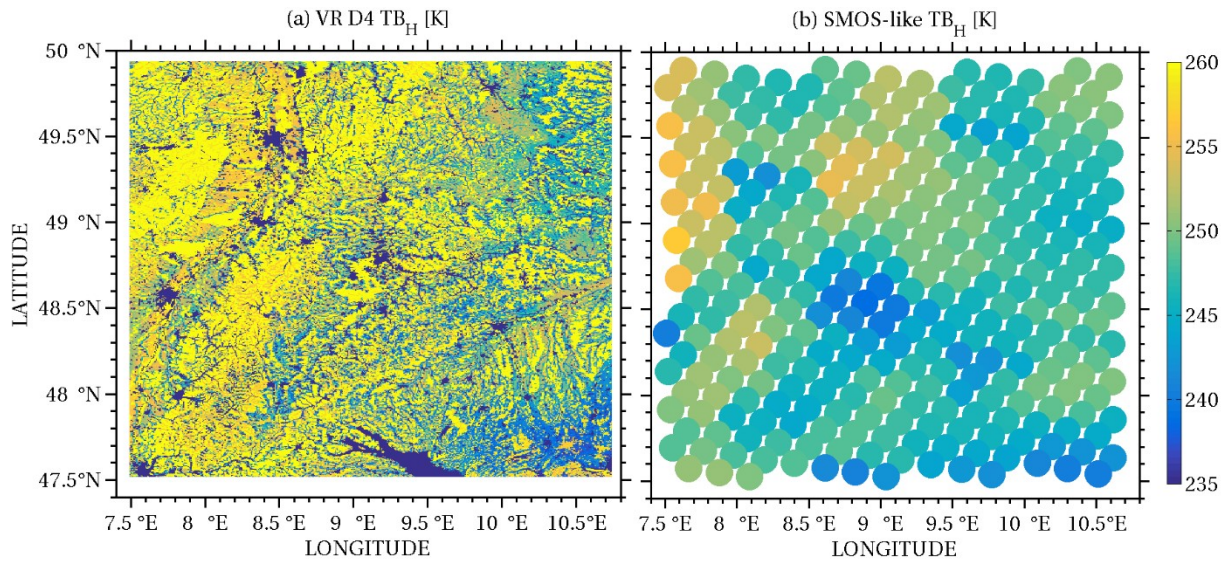


973

974 Figure A2: Snapshot of the three dimensional distribution of cloud water/ice [g/kg] (greyscale), precipitation/rain water [g/kg]

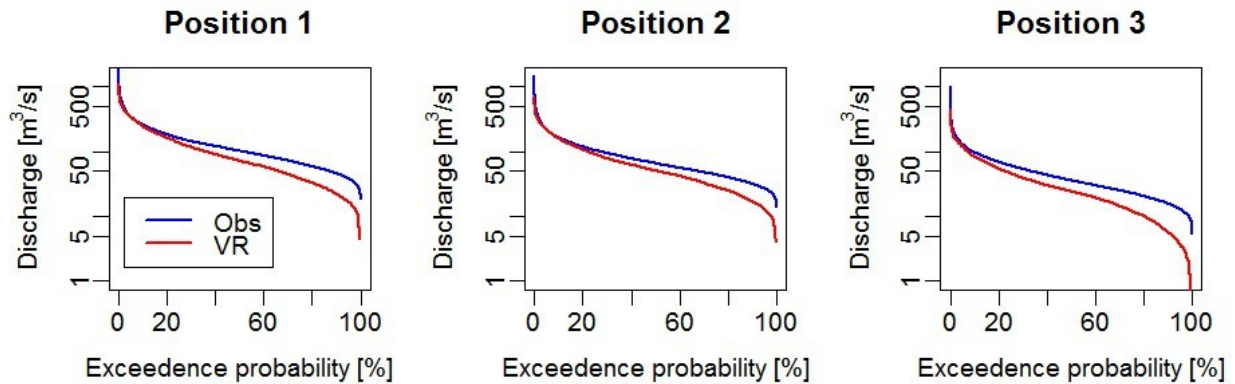
975 (blue in foreground over cloud) and soil moisture [cm³/cm³] (colored) at a time point with a single rain cloud with light rain.

976



977

978 **Figure A3: Brightness temperature calculated by the application of CMEM (H-polarization) on the simulated-reality output on**
 979 **July 2nd 2011 (left) and its aggregation on the spatial resolution of the L1C data-product SMOS passive microwave radiometer**
 980 **(right).**



981

982 **Figure A4: Flow duration curve for the three stations for the three-year time period based on. Blue: observations; red: simulated**
 983 **catchment.**

984